SYNTHESIS, CHARACTERIZATION, NUCLEOLYTIC, ANTIBACTERIAL AND ANTIPROLIFERATIVE PROPERTIES OF VANADIUM, COPPER AND MANGANESE COMPLEXES

LIM ENG KHOON

Thesis submitted in fulfillment of the requirements

for the degree of

Doctor of Philosophy

July 2011

ACKNOWLEDGEMENTS

I would like to express profound gratitude to my supervisor, Professor Dr. Teoh Siang Guan, for his invaluable support, encouragement, enthusiasm, supervision and useful suggestions throughout this research work. His moral support and continuous guidance enabled me to complete my work successfully. I am also highly thankful to Associate Professor Dr. Ng Chew Hee, Faculty of Engineering and Science, Universiti Tunku Abdul Rahman, Professor Dr. Mohd Nazalan Mohd Najimudin, School of Biological Sciences, Universiti Sains Malaysia and Professor Dr. Tengku Sifzizul Tengku Muhammad, School of Biological Sciences, Universiti Sains Malaysia, for their valuable suggestions throughout this study.

I would also like to express my deep appreciation to Professor Dr. Fun Hoong Kun and Mr. Mohd Mustaqim Rosli, X-ray Crystallography Unit, School of Physics, Universiti Sains Malaysia, for their professional guidance, excellent help and valuable advice for running and analysis all my X-ray Crystallography samples.

Special thanks go to Miss Beh Hooi Kheng and Miss Seow Lay Jing, School of Pharmaceutical Sciences, Universiti Sains Malaysia; Mr. Cheah Yew Hoong, Bioassay Unit, Herbal Medicine Research Center, Institute Medical Centre; Miss Chew Guat Siew, Mr. Yam Hok Chai, Mr. Yuen Chee Wah and Mr. Emmanuel Jairaj Moses, School of Biological Sciences, Universiti Sains Malaysia, for their guidance and help in the biological tests.

I want to give my thanks to the staff of the School of Chemical Science, Universiti Sains Malaysia, especially to Mr. Aw Yeong Choek Hoe, Mr. Ong Chin Hwie, Mr. Ong Ching Hin, Mr. Razli Effendy bin Khalidee, Mr. Marimuthu Ayeroo, Pn. Hjh. Zali Zaiton Hj. Hussin, Pn. Yeoh Chooi Ling, Mr. Ahmad Azrulhisham Abdul Rahim, Mr. Mohd Kassim Abd Razak, Mr. Yee Chin Leng and Mr. Clement D' Silva, for their constant help and support throughout my study.

I am also sincerely grateful to USM Fellowship award from Institute of Postgraduate Studies (IPS), Universiti Sains Malaysia, for the financial support and RU Grant and Science Fund from Universiti Sains Malaysia, and FRGS Grant from Ministry of Higher Education (MOHE), Malaysia, for funding this research.

I also like to express my warmest gratitude to my friends, especially to Sharon Fatinathan, Yasodha Sivasothy, Ong Chin Hin, Oo Chuan Wei, Vijay, Yoga, Wendy, Mandy, Cynn Dee, William Yip, Karen Onn and many more, for their moral support and kindness.

Finally, I would like to thank my family members, especially my wife, Belle, for supporting and encouraging me to pursue this degree. Without my family encouragement, I would not have finished the degree.

To all of you, I say *Ribuan Terima Kasih*

TABLE OF CONTENTS

	Page
Title page	i
Acknowledgements	ii
Table of Contents	iv
List of Figures	xi
List of Tables	xxxv
List of Abbreviations and Symbols	xlii
Abstract in Bahasa Malaysia	xlv
Abstract in English	xlvii
CHAPTER 1 INTRODUCTION	1
1.1 Biological roles and medicinal applications of metal complexes and metal ions	1
1.2 Antibacterial and antiproliferative activities of transition metal complexes	4
1.3 Background of nucleolytic activity of metal complexes	7
1.3.1 Oxidative DNA cleavage by metal complexes in the presence of 3-mercaptopropionic acid (MPA)	12
1.3.2 Oxidative DNA cleavage by metal complexes in the presence of ascorbic acid	14
1.3.3 Oxidative DNA cleavage by metal complexes in the presence of H_2O_2	16
1.3.4 Photolytic DNA cleavage by metal complexes	18
1.3.5 Hydrolytic DNA cleavage by metal complexes	21
1.3.6 Oxidative DNA cleavage by copper(II) amino acid complexes in the presence of H_2O_2	23
1.4 DNA-metal complexes interaction	25
1.5 Research Objective	27

TABLE OF CONTENTS

Page

CHAPTER 2 EXPERIMENTAL 29

2.1 Reagents and materials 29

2.2 Instruments 29

2.3 X-ray crystallography 31

2.4 DNA cleavage experiments 31

2.5 DNA binding absorption studies 32

2.6 Antibacterial screening (inhibition zone) 33

2.7 Antibacterial screening (MIC) 33

2.8 Cell line and cell culture 34

2.9 In vitro cytotoxic assay (Sulforhodamine B (SRB)) 34

2.10 MTT (3-[4,5-dimethylthiazol-2-yl]-2,5-diphenyl tetrazolium bromide) assay 36

2.11 Synthesis 37

2.11.1 Synthesis of complex **VO$_2$PP** 38

2.11.2 Synthesis of complex **VO$_2$GLY** 39

2.11.3 Synthesis of complex **VOPYDC** 39

2.11.4 Synthesis of complex **VOMAL** 40

2.11.5 Synthesis of complex **VO$_2$HPYDC** 40

2.11.6 Synthesis of complexes **Cu-4-Cl-2-NO$_2$BZO**, **Cu-2-Cl-6-FBZO**, **Cu-2-ClBZO** and **Cu-2-BrBZO** 41

2.11.7 Synthesis of complexes **Cu-2-Cl-4-NO$_2$BZO**, **CuP-5-Cl-2-NO$_2$BZO** and **Cu-2-F-6-FBZO** 42

TABLE OF CONTENTS

Page

2.11.8 Synthesis of complexes **MnP-4-Cl-2-NO$_2$BZO**, **MnP-3-NO$_2$-5-NO$_2$BZO**, **Mn-4-NO$_2$BZO**, **MnP-4-NH$_2$BZO**, **MnP-4-FBZO**, **MnP-4-ClBZO** and **MnPGLY** 44

2.11.9 Synthesis of complex **MnPyr** 46

2.11.10 Synthesis of complexes **VOPhen**, **VODMPhen**, **VODPPhen** and **VODMPPhen** 46

CHAPTER 3 **Characterization, Nucleolytic, Antibacterial and Antiproliferative Properties of Vanadium Carboxylato Complexes** 48

Results and Discussion

3.1 X-ray crystallography analysis of complex VO$_2$PP 48

3.2 X-ray crystallography analysis of complex VO$_2$GLY 53

3.3 X-ray crystallography analysis of complex VOPYDC 58

3.4 FT-IR analysis of complexes VO$_2$PP, VO$_2$GLY and VO$_2$HPYDC 63

3.5 FT-IR analysis of complexes VOPYDC and VOMAL 69

3.6 UV-Vis analysis of complexes VO$_2$PP, VO$_2$GLY, VO$_2$HPYDC, VOPYDC and VOMAL 74

3.7 ^{51}V-NMR analysis of complexes VO$_2$PP, VO$_2$GLY, VO$_2$HPYDC, VOPYDC and VOMAL 83

3.8 Redox property of complexes VO$_2$PP, VO$_2$GLY, VOPYDC, VOMAL and VO$_2$HPYDC 88

3.9 DNA cleavage activity of complexes VO$_2$PP, VO$_2$GLY, VOPYDC, VOMAL and VO$_2$HPYDC 93

3.10 Comparison of DNA cleavage activity of complexes VO$_2$PP, VO$_2$GLY, VOPYDC, VOMAL and VO$_2$HPYDC 100

TABLE OF CONTENTS

Page

3.11 DNA cleavage mechanism study of complexes VO$_2$PP, VO$_2$GLY, VOPYDC, VOMAL and VO$_2$HPYDC 102

3.12 Antibacterial activity of complexes VO$_2$PP, VO$_2$GLY, VOPYDC, VOMAL and VO$_2$HPYDC 107

3.13 Antiproliferative activity of complexes VO$_2$PP, VO$_2$GLY, VOPYDC, VOMAL and VO$_2$HPYDC 110

CHAPTER 4 **Characterization, Nucleolytic, Antibacterial and Antiproliferative Properties of Copper Carboxylato Complexes** 113

4.1 X-ray crystallography analysis of complexes Cu-4-Cl-2-NO$_2$BZO, Cu-2-Cl-4-NO$_2$BZO, Cu-2-Cl-6-FBZO, Cu-2-F-6-FBZO, Cu-2-ClBZO and Cu-2-BrBZO 113

4.2 X-ray crystallography analysis of complex CuP-5-Cl-2-NO$_2$BZO 136

4.3 FT-IR analysis of complexes Cu-4-Cl-2-NO$_2$BZO, Cu-2-Cl-4-NO$_2$BZO, CuP-5-Cl-2-NO$_2$BZO, Cu-2-Cl-6-FBZO, Cu-2-F-6-FBZO, Cu-2-ClBZO and Cu-2-BrBZO 142

4.4 UV-Vis analysis of complexes Cu-4-Cl-2-NO$_2$BZO, Cu-2-Cl-4-NO$_2$BZO, CuP-5-Cl-2-NO$_2$BZO, Cu-2-Cl-6-FBZO, Cu-2-F-6-FBZO, Cu-2-ClBZO and Cu-2-BrBZO 153

4.5 Redox property of complexes Cu-4-Cl-2-NO$_2$BZO, Cu-2-Cl-4-NO$_2$BZO, CuP-5-Cl-2-NO$_2$BZO, Cu-2-Cl-6-FBZO, Cu-2-F-6-FBZO, Cu-2-ClBZO and Cu-2-BrBZO 163

4.6 DNA cleavage activity of complexes Cu-4-Cl-2-NO$_2$BZO, Cu-2-Cl-4-NO$_2$BZO, CuP-5-Cl-2-NO$_2$BZO, Cu-2-Cl-6-FBZO, Cu-2-F-6-FBZO, Cu-2-ClBZO and Cu-2-BrBZO 168

4.7 Comparison of DNA cleavage activity of complexes Cu-4-Cl-2-NO$_2$BZO, Cu-2-Cl-4-NO$_2$BZO, CuP-5-Cl-2-NO$_2$BZO, Cu-2-Cl-6-FBZO, Cu-2-F-6-FBZO, Cu-2-ClBZO and Cu-2-BrBZO 176

TABLE OF CONTENTS

Page

4.8 DNA cleavage mechanism studies of complexes Cu-4-Cl-2-NO_2BZO, Cu-2-Cl-4-NO_2BZO, CuP-5-Cl-2-NO_2BZO, Cu-2-Cl-6-FBZO, Cu-2-F-6-FBZO, Cu-2-ClBZO and Cu-2-BrBZO 178

4.9 Antibacterial activity of complexes Cu-4-Cl-2-NO_2BZO, Cu-2-Cl-4-NO_2BZO, CuP-5-Cl-2-NO_2BZO, Cu-2-Cl-6-FBZO, Cu-2-F-6-FBZO, Cu-2-ClBZO and Cu-2-BrBZO 184

4.10 Antiproliferative activity of complexes Cu-4-Cl-2-NO_2BZO, Cu-2-Cl-4-NO_2BZO, CuP-5-Cl-2-NO_2BZO, Cu-2-Cl-6-FBZO, Cu-2-F-6-FBZO and Cu-2-ClBZO 188

CHAPTER 5 Characterization, Nucleolytic, Antibacterial and Antiproliferative Properties of Manganese Carboxylato Complexes 192

Results and Discussion

5.1 X-ray crystallography analysis of complexes MnP-4-Cl-2-NO_2BZO, MnP-3-NO_2-5-NO_2BZO and Mn-4-NO_2BZO 192

5.2 X-ray crystallography analysis of complex MnP-4-NH_2BZO 203

5.3 X-ray crystallography analysis of complex MnP-4-FBZO 208

5.4 X-ray crystallography analysis of complex MnPGLY 213

5.5 FT-IR analysis of complexes MnP-4-Cl-2-NO_2BZO, MnP-3-NO_2-5-NO_2BZO, Mn-4-NO_2BZO, MnP-4-NH_2BZO, MnP-4-FBZO, MnP-4-ClBZO, MnPGLY and MnPyr 218

5.6 UV-Vis analysis of complexes MnP-4-Cl-2-NO_2BZO, MnP-3-NO_2-5-NO_2BZO, Mn-4-NO_2BZO, MnP-4-NH_2BZO, MnP-4-FBZO, MnP-4-ClBZO, MnPGLY and MnPyr 231

5.7 Redox property of complexes MnP-4-Cl-2-NO_2BZO, MnP-3-NO_2-5-NO_2BZO, Mn-4-NO_2BZO, MnP-4-NH_2BZO, MnP-4-FBZO, MnP-4-ClBZO, MnPGLY and MnPyr 242

TABLE OF CONTENTS

Page

5.8 DNA cleavage activity of complexes MnP-4-Cl-2-NO_2BZO, MnP-3-NO_2-5-NO_2BZO, Mn-4-NO_2BZO, MnP-4-NH_2BZO, MnP-4-FBZO, MnP-4-ClBZO, MnPGLY and MnPyr 249

5.9 Comparison of DNA cleavage activity of complexes MnP-4-Cl-2-NO_2BZO, MnP-3-NO_2-5-NO_2BZO, Mn-4-NO_2BZO, MnP-4-NH_2BZO, MnP-4-FBZO, MnP-4-ClBZO, MnPGLY and MnPyr 258

5.10 DNA cleavage mechanism studies of complexes MnP-4-Cl-2-NO_2BZO, MnP-3-NO_2-5-NO_2BZO, Mn-4-NO_2BZO, MnP-4-NH_2BZO, MnP-4-FBZO, MnP-4-ClBZO, MnPGLY and MnPyr 260

5.11 Antibacterial activity of complexes MnP-4-Cl-2-NO_2BZO, MnP-3-NO_2-5-NO_2BZO, Mn-4-NO_2BZO, MnP-4-NH_2BZO, MnP-4-FBZO, MnP-4-ClBZO, MnPGLY and MnPyr 265

5.12 Antiproliferative activity of complexes MnP-4-Cl-2-NO_2BZO, MnP-3-NO_2-5-NO_2BZO, Mn-4-NO_2BZO, MnP-4-NH_2BZO and MnPyr 268

CHAPTER 6 Characterization, Nucleolytic, Antibacterial and Antiproliferative Properties of Vanadium(IV) Phenanthroline Derivative Complexes 270

Results and Discussion

6.1 Characterization of complexes VOPhen, VODMPhen, VODPPhen and VODMPPhen 270

6.2 DNA binding studies 278

  6.2.1 Electronic absorption spectra study of complexes **VOPhen**, **VODMPhen**, **VODPPhen** and **VODMPPhen** 278

  6.2.2 Viscosity study of complexes **VOPhen**, **VODMPhen**, **VODPPhen** and **VODMPPhen** 288

  6.2.3 Circular dichroism (CD) study of complexes **VOPhen**, **VODMPhen**, **VODPPhen** and **VODMPPhen** 290

TABLE OF CONTENTS

Page

6.3 DNA cleavage activity of complexes **VOPhen**, **VODMPhen**, **VODPPhen** and **VODMPPhen** 291

6.4 Comparison of DNA cleavage activity of complexes **VOPhen**, **VODMPhen**, **VODPPhen** and **VODMPPhen** 296

6.5 Antibacterial and antiproliferative activities of complexes **VOPhen**, **VODMPhen**, **VODPPhen** and **VODMPPhen** 300

6.6 The insight of antibacterial and antiproliferative activities of vanadium carboxylato complexes and vanadium phenanthroline derivative complexes 304

CHAPTER 7 CONCLUSION 306

REFERENCES 307

APPENDICES 318

PUBLICATIONS 320

LIST OF FIGURES

		Page
Figure 1.1	Schematic structures of cisplatin, carboplatin and oxaliplatin	2
Figure 1.2	The structure of part of a DNA double helix	8
Figure 1.3	The chemical structure of DNA. Hydrogen bonds are shown as dotted lines.	9
Figure 1.4	Supercoiled, nicked and linear DNA	11
Figure 1.5	Supercoiled, nicked and linear DNA bands in gel electrophoresis diagram	12
Figure 1.6	The schematic structures; a)[Cu^{II}(ternary-L-glutamine)(1,10-phenanthroline)(H_2O)](ClO_4) b)[Cu^{II}(ternary-S-methyl-L-cysteine)(1,10-phenanthroline)(H_2O)](ClO_4)	13
Figure 1.7	The proposed DNA cleavage mechanism of metal complex in the presence of 3-mercaptopropionic acid (MPA)	13
Figure 1.8	The schematic structures; a) [Ru^{II}(imidazo[4,5-f][1,10]phenanthroline)(NH_3)$_4$](PF_6)$_2$ b) [Cu^{II}(L-threonine)(1,10-phenanthroline) (H_2O)](ClO_4)	15
Figure 1.9	The proposed DNA cleavage mechanism of metal complex in the presence of ascorbic acid	15
Figure 1.10	The schematic structures; a) [Co^{II}(imidazole-terpyridine)$_2$](ClO_4)$_2$ b) [Cu^{II}(imidazole terpyridine)$_2$](ClO_4)$_2$	17
Figure 1.11	The proposed DNA cleavage mechanism of metal complex in the presence of H_2O_2	17
Figure 1.12	The schematic structures; a) [Cu^{II} (ternary-S-methyl-L-cysteine)(dipyridoquinoxaline)(H_2O)](ClO_4) b) [Co^{III}(ethylenediamine)$_2$(imidazo[4,5-f][1,10]-phenanthroline)]Br_3	19

LIST OF FIGURES

		Page
Figure 1.12	The schematic structures; c) [Ru^{II}(2,2'-bipyridine)$_2$(5-methoxy-isatino-[1,2-b]-1,4,8,9-tetraazatriphenylene)](ClO$_4$)$_2$ d) [Ni^{II}(naptho[2,3-*a*]dipyrido[3,2-*h*:2',3'-*f*]phenazine-5,18-dione)(1,10-phenanthroline)](PF$_6$)	20
Figure 1.13	The proposed DNA cleavage mechanism of metal complex upon irradiation	21
Figure 1.14	The schematic structures; a) [Co^{III}(bis[2-(2-pyridylethyl)]-(2-pyridylmethyl)amine)(OH)(H$_2$O)]$^{2+}$ b) [Mn^{II}(quercetin)$_2$(H$_2$O)$_2$]Cl$_2$	22
Figure 1.15	The proposed hydrolytic DNA cleavage mechanism by the metal complex	23
Figure 1.16	The schematic structures; a) Cu^{II}(N,N'-dimethylglycinato)$_2$ b) Cu^{II}(*N,N*-di-(*N*'-methylacetamido)-L-alaninato)$_2$	24
Figure 1.17	Complexes bind with DNA via hydrogen bonding	25
Figure 1.18	Complexes bind with DNA via electrostatic interaction	26
Figure 1.19	Complexes binds with DNA via intercalation	26
Figure 3.1	The molecular structure of complex **VO$_2$PP**, showing 50 % probability displacement ellipsoids and the atomic numbering (Refer to the list of Publication at page 325)	50
Figure 3.2	The crystal packing of complex **VO$_2$PP**	51
Figure 3.3	The molecular structure of complex **VO$_2$GLY**, showing 50 % probability displacement ellipsoids and the atomic numbering	55
Figure 3.4	The crystal packing of complex **VO$_2$GLY**	56

LIST OF FIGURES

Page

Figure 3.5 The molecular structure of complex **VOPYDC**, showing 50 % probability displacement ellipsoids and the atomic numbering (Refer to the list of Publication at page 325) 60

Figure 3.6 The crystal packing of complex **VOPYDC** 61

Figure 3.7(A) FT-IR spectrum of complex **VO$_2$PP** 66

Figure 3.7(B) FT-IR spectrum of 2-picolinic acid 66

Figure 3.8(A) FT-IR spectrum of complex **VO$_2$GLY** 67

Figure 3.8(B) FT-IR spectrum of diglycolic acid 67

Figure 3.9 Chemical structure of complex **VO$_2$HPYDC** [72] 68

Figure 3.10(A) FT-IR spectrum of complex **VO$_2$HPYDC** 68

Figure 3.10(B) FT-IR spectrum of 4-hydroxypyridine-2,6-dicarboxylic acid 69

Figure 3.11(A) FT-IR spectrum of complex **VOPYDC** 72

Figure 3.11(B) FT-IR spectrum of pyridine-2,6-dicarboxylic acid 72

Figure 3.12 Chemical structure of complex **VOMAL** [71] 73

Figure 3.13(A) FT-IR spectrum of complex **VOMAL** 73

Figure 3.13(B) FT-IR spectrum of malonic acid 74

Figure 3.14(A) UV-Vis spectrum of complex **VO$_2$PP** (9.94×10^{-3} mol L^{-1}) 77

Figure 3.14(B) UV-Vis spectrum of complex **VO$_2$PP** (3.96×10^{-5} mol L^{-1}; A = 262 nm, ε =10 295 mol^{-1}Lcm^{-1}; A = 204 nm, ε = 20 485 mol^{-1}Lcm^{-1}) 77

Figure 3.15(A) UV-Vis spectrum of complex **VO$_2$GLY** (0.014 mol L^{-1}) 78

Figure 3.15(B) UV-Vis spectrum of complex **VO$_2$GLY** (5.47×10^{-5} mol L^{-1}; A = 259 nm, ε = 2945 mol^{-1}Lcm^{-1}; A = 203 nm, ε = 7310 mol^{-1}Lcm^{-1}) 78

LIST OF FIGURES

Page

Figure 3.16(A) UV-Vis spectrum of complex **VO_2HPYDC** (0.012 mol L^{-1}) 79

Figure 3.16(B) UV-Vis spectrum of complex **VO_2HPYDC** (9.18 x 10^{-6} mol L^{-1}; A = 276 nm, ε = 12 730 $mol^{-1}Lcm^{-1}$; A = 203 nm, ε = 44 762 $mol^{-1}Lcm^{-1}$) 79

Figure 3.17(A) UV-Vis spectrum of complex **VOPYDC** (0.013 mol L^{-1}; A = 836 nm, ε = 26 $mol^{-1}Lcm^{-1}$; A = 616 nm, ε = 16 $mol^{-1}Lcm^{-1}$) 80

Figure 3.17(B) UV-Vis spectrum of complex **VOPYDC** (2.57 x 10^{-5} mol L^{-1}; A = 268 nm, ε = 5512 $mol^{-1}Lcm^{-1}$; A = 207 nm, ε = 18 648 $mol^{-1}Lcm^{-1}$) 80

Figure 3.18(A) UV-Vis spectrum of complex **VOMAL** (0.011 mol L^{-1}; A = 804 nm, ε = 36 $mol^{-1}Lcm^{-1}$; A = 595 nm, ε = 12 $mol^{-1}Lcm^{-1}$) 81

Figure 3.18(B) UV-Vis spectrum of complex **VOMAL** (4.45 x 10^{-5} mol L^{-1}; A = 263 nm, ε = 1689 $mol^{-1}Lcm^{-1}$; A = 203 nm, ε = 8025 $mol^{-1}Lcm^{-1}$) 81

Figure 3.19 UV-Vis spectrum of $NaVO_3$ (0.016 mol L^{-1}) 82

Figure 3.20 UV-Vis spectrum of $VOSO_4$ (0.024 mol L^{-1}**;** A = 777 nm, ε = 11 $mol^{-1}Lcm^{-1}$; A = 614 nm, ε = 5 $mol^{-1}Lcm^{-1}$) 82

Figure 3.21(A) ^{51}V-NMR spectrum of complex **VO_2PP** (300.0 K) 85

Figure 3.21(B) ^{51}V-NMR spectrum of complex **VO_2GLY** (300.0 K) 85

Figure 3.21(C) ^{51}V-NMR spectrum of complex **VO_2HPYDC** (300.0 K) 86

Figure 3.21(D) ^{51}V-NMR spectrum of complex **VOPYDC** (300.0 K) 86

Figure 3.21(E) ^{51}V-NMR spectrum of complex **VOMAL** (300.0 K) 87

Figure 3.22 :^{51}V-NMR spectrum of $NaVO_3$ (300.0 K) 87

Figure 3.23 :^{51}V-NMR spectrum of complex $VOSO_4$ (300.0 K) 88

LIST OF FIGURES

		Page
Figure 3.24(A)	Cyclic voltammogram of complex **VO_2PP**; Epa = anodic oxidation peak, Epc = cathodic reduction peak	90
Figure 3.24(B)	Cyclic voltammogram of complex **VO_2GLY**; Epa = anodic oxidation peak, Epc = cathodic reduction peak	91
Figure 3.24(C)	Cyclic voltammogram of complex **VOPYDC**; Epa = anodic oxidation peak, Epc = cathodic reduction peak	91
Figure 3.24(D)	Cyclic voltammogram of complex **VOMAL**; Epa = anodic oxidation peak, Epc = cathodic reduction peak	92
Figure 3.24(E)	Cyclic voltammogram of complex **VO_2HPYDC**; Epa = anodic oxidation peak, Epc = cathodic reduction peak	92
Figure 3.25	Cleavage of supercoiled pBR322 by complex **VO_2PP** at different concentrations in phosphate buffer pH 7.5. L1 Gene Ruler 1 kb DNA ladder, L2, DNA alone; L3, H_2O_2 alone; L4, complex alone (6 mM); Lanes 5-12 DNA with increasing concentration of complex + H_2O_2: lane 5, 10 μM; lane 6, 50 μM; lane 7, 1 mM; lane 8, 2 mM; lane 9, 3 mM; lane 10, 4 mM; lane 11, 5 mM; lane 12, 6 mM.	94
Figure 3.26	Gene Ruler 1 kb DNA ladder, unit in bp (base pair)	95
Figure 3.27	Cleavage of supercoiled pBR322 by complex **VO_2GLY** at different concentrations in phosphate buffer pH 7.5. L1 Gene Ruler 1 kb DNA ladder, L2, DNA alone; L3, H_2O_2 alone; L4, complex alone (6 mM); Lanes 5-12 DNA with increasing concentration of complex + H_2O_2: lane 5, 10 μM; lane 6, 50 μM; lane 7, 1 mM; lane 8, 2 mM; lane 9, 3 mM; lane 10, 4 mM; lane 11, 5 mM; lane 12, 6 mM.	96
Figure 3.28	Cleavage of supercoiled pBR322 by complex **VOPYDC** at different concentrations in phosphate buffer pH 7.5. L1 Gene Ruler 1 kb DNA ladder, L2 DNA alone, Lanes 3-12 DNA with increasing concentration of complex: lane 3, 50 μM; lane 4, 100 μM; lane 5, 200 μM; lane 6, 300 μM; lane 7, 400 μM; lane 8, 500 μM; lane 9, 600 μM; lane 10, 700 μM; lane 11, 800 μM; lane 12, 900 μM.	97
Figure 3.29	Cleavage of supercoiled pBR322 by complex **VOMAL** at different concentrations in phosphate buffer pH 7.5. L1 Gene Ruler 1 kb DNA ladder, L2 DNA alone, Lanes 3-12 DNA with increasing concentration of complex: lane 3, 50 μM; lane 4, 100 μM; lane 5, 200 μM; lane 6, 300 μM; lane 7, 400 μM; lane 8, 500 μM; lane 9, 600 μM; lane 10, 700 μM; lane 11, 800 μM; lane 12, 900 μM.	98

LIST OF FIGURES

Page

Figure 3.30(A) Cleavage of supercoiled pBR322 by complex **VO_2HPYDC** at different concentrations in phosphate buffer pH 7.5. L1 Gene Ruler 1 kb DNA ladder, L2, DNA alone; L3, H_2O_2 alone; L4, complex alone (6 mM); Lanes 5-12 DNA with increasing concentration of complex + H_2O_2: lane 5, 10 µM; lane 6, 50 µM; lane 7, 1 mM; lane 8, 2 mM; lane 9, 3 mM; lane 10, 4 mM; lane 11, 5 mM; lane 12, 6 mM. 99

Figure 3.30(B) Cleavage of supercoiled pBR322 by complex **VO_2HPYDC** at different concentrations in phosphate buffer pH 7.5. L1 Gene Ruler 1 kb DNA ladder, L2, DNA alone; L3, H_2O_2 alone; L4, complex alone (14 mM); Lanes 5-12 DNA with increasing concentration of complex + H_2O_2: lane 5, 7 mM; lane 6, 8 mM; lane 7, 9 mM; lane 8, 10 mM; lane 9, 11 mM; lane 10, 12 mM; lane 11, 13 mM; lane 12, 14 mM. 99

Figure 3.31 Cleavage of supercoiled pBR322 by $NaVO_3$ at different concentrations in phosphate buffer pH 7.5. L1 Gene Ruler 1 kb DNA ladder, L2, DNA alone; L3, H_2O_2 alone; L4, $NaVO_3$ alone (14 mM); Lanes 5-12 DNA with increasing concentration of $NaVO_3$ + H_2O_2: lane 5, 7 mM; lane 6, 8 mM; lane 7, 9 mM; lane 8, 10 mM; lane 9, 11 mM; lane 10, 12 mM; lane 11, 13 mM; lane 12, 14 mM. 101

Figure 3.32 Cleavage of supercoiled pBR322 by $VOSO_4$ at different concentrations in phosphate buffer pH 7.5. L1 Gene Ruler 1 kb DNA ladder, L2 DNA alone, Lanes 3-12 DNA with increasing concentration of $VOSO_4$: lane 3, 50 µM; lane 4, 100 µM; lane 5, 200 µM; lane 6, 300 µM; lane 7, 400 µM; lane 8, 500 µM; lane 9, 600 µM; lane 10, 700 µM; lane 11, 800 µM; lane 12, 900 µM. 102

Figure 3.33 Effect of various scavengers on the cleavage of pBR322 by 2 mM complex **VO_2PP**. Lane 1, Gene Ruler 1 kb DNA ladder; Lane 2, DNA alone; Lane 3, DNA + 2 mM complex **VO_2PP** + H_2O_2. Lanes 4 – 12 involves reaction of 2 mM complex **VO_2PP** + H_2O_2 with DNA in presence of various scavengers; lane 4, t-butyl alcohol (1 M); lane 5, 1 mM Mannitol; lane 6, DMSO (1 M); lane 7, 1 mM NaN_3; lane 8, 10 mM NaN_3; lane 9, 20 mM NaN_3; lane 10, 30 mM NaN_3; lane 11, 50 mM NaN_3; lane 12, 100 mM NaN_3. 104

Figure 3.34 Effect of various scavengers on the cleavage of pBR322 by 6 mM complex **VO_2GLY**. Lane 1, Gene Ruler 1 kb DNA ladder; Lane 2, DNA alone; Lane 3, DNA + 6 mM complex **VO_2GLY** + H_2O_2. Lanes 4 – 12 involves reaction of 6 mM complex **VO_2GLY** + H_2O_2 with DNA in presence of various scavengers; lane 4, t-butyl alcohol (1 M); lane 5, 1 mM Mannitol; lane 6, DMSO (1 M); lane 7, 1 mM NaN_3; lane 8, 10 mM NaN_3; lane 9, 20 mM NaN_3; lane 10, 30 mM NaN_3; lane 11, 50 mM NaN_3; lane 12, 100 mM NaN_3. 104

LIST OF FIGURES

Page

Figure 3.35 Effect of various scavengers on the cleavage of pBR322 by 7 mM complex **VO_2HPYDC**. Lane 1, Gene Ruler 1 kb DNA ladder; Lane 2, DNA alone; Lane 3, DNA + 7 mM complex **VO_2HPYDC** + H_2O_2. Lanes 4 – 12 involves reaction of 7 mM complex **VO_2HPYDC** + H_2O_2 with DNA in presence of various scavengers; lane 4, t-butyl alcohol (1 M); lane 5, 1 mM Mannitol; lane 6, DMSO (1 M); lane 7, 1 mM NaN_3; lane 8, 10 mM NaN_3; lane 9, 20 mM NaN_3; lane 10, 30 mM NaN_3; lane 11, 50 mM NaN_3; lane 12, 100 mM NaN_3. 105

Figure 3.36 Effect of various scavengers on the cleavage of pBR322 by 200 μM complex **VOPYDC**. Lane 1, Gene Ruler 1 kb DNA ladder; Lane 2, DNA alone; Lane 3, DNA + 200 μM complex **VOPYDC**. Lanes 4 – 12 involves reaction of 200 μM complex **VOPYDC** with DNA in presence of various scavengers; lane 4, t-butyl alcohol (1 M); lane 5, 1 mM Mannitol; lane 6, DMSO (1 M); lane 7, 1 mM NaN_3; lane 8, 10 mM NaN_3; lane 9, 20 mM NaN_3; lane 10, 30 mM NaN_3; lane 11, 50 mM NaN_3; lane 12, 100 mM NaN_3. 105

Figure 3.37 Effect of various scavengers on the cleavage of pBR322 by 400 μM complex **VOMAL**. Lane 1, Gene Ruler 1 kb DNA ladder; Lane 2, DNA alone; Lane 3, DNA + 400 μM complex **VOMAL**. Lanes 4 – 12 involves reaction of 400 μM complex **VOMAL** with DNA in presence of various scavengers; lane 4, t-butyl alcohol (1 M); lane 5, 1 mM Mannitol; lane 6, DMSO (1 M); lane 7, 1 mM NaN_3; lane 8, 10 mM NaN_3; lane 9, 20 mM NaN_3; lane 10, 30 mM NaN_3; lane 11, 50 mM NaN_3; lane 12, 100 mM NaN_3. 106

Figure 3.38 The proposed DNA cleavage mechanism of complexes **VO_2PP**, **VO_2GLY** and **VO_2HPYDC** in the presence of H_2O_2 106

Figure 3.39 The proposed DNA cleavage mechanism of complexes **VOPYDC** and **VOMAL** in the absence of H_2O_2 107

Figure 4.1 The molecular structure of complex **Cu-4-Cl-2-NO_2BZO**, showing 50 % probability displacement ellipsoids and the atomic numbering (Refer to the list of Publication at page 325) 118

Figure 4.2 The crystal packing of complex **Cu-4-Cl-2-NO_2BZO** 119

Figure 4.3 The molecular structure of complex **Cu-2-Cl-4-NO_2BZO**, showing 50 % probability displacement ellipsoids and the atomic numbering (Refer to the list of Publication at page 325) 121

Figure 4.4 The crystal packing of complex **Cu-2-Cl-4-NO_2BZO** 122

LIST OF FIGURES

		Page
Figure 4.5	The molecular structure of complex **Cu-2-Cl-6-FBZO**, showing 50 % probability displacement ellipsoids and the atomic numbering (Refer to the list of Publication at page 325)	124
Figure 4.6	The crystal packing of complex **Cu-2-Cl-6-FBZO**	125
Figure 4.7	The molecular structure of complex **Cu-2-F-6-FBZO**, showing 50 % probability displacement ellipsoids and the atomic numbering (Refer to the list of Publication at page 325)	127
Figure 4.8	The crystal packing of complex **Cu-2-F-6-FBZO**	128
Figure 4.9	The molecular structure of complex **Cu-2-ClBZO**, showing 50 % probability displacement ellipsoids and the atomic numbering	130
Figure 4.10	The crystal packing of complex **Cu-2-ClBZO**	131
Figure 4.11	The molecular structure of complex **Cu-2-BrBZO**, showing 50 % probability displacement ellipsoids and the atomic numbering	133
Figure 4.12	The crystal packing of complex **Cu-2-BrBZO**	134
Figure 4.13	The partial polymeric structure of complex **CuP-5-Cl-2-NO_2BZO**, showing 50 % probability displacement ellipsoids and the atomic numbering (Refer to the list of Publication at page 325)	138
Figure 4.14	The chemical structure of polymeric complex **CuP-5-Cl-2-NO_2BZO**	139
Figure 4.15	The crystal packing of polymeric complex **CuP-5-Cl-2-NO_2BZO**	140
Figure 4.16(A)	FT-IR spectrum of complex **Cu-4-Cl-2-NO_2BZO**	146
Figure 4.16(B)	FT-IR spectrum of 4-chloro-2-nitrobenzoic acid	146
Figure 4.17(A)	FT-IR spectrum of complex **Cu-2-Cl-4-NO_2BZO**	147
Figure 4.17(B)	FT-IR spectrum of 2-chloro-4-nitrobenzoic acid	147

LIST OF FIGURES

Page

Figure 4.18(A) FT-IR spectrum of complex **CuP-5-Cl-2-NO$_2$BZO** 148

Figure 4.18(B) FT-IR spectrum of 5-chloro-2-nitrobenzoic acid 148

Figure 4.19(A) FT-IR spectrum of complex **Cu-2-Cl-6-FBZO** 149

Figure 4.19(B) FT-IR spectrum of 2-chloro-6-fluorobenzoic acid 149

Figure 4.20(A) FT-IR spectrum of complex **Cu-2-F-6-FBZO** 150

Figure 4.20(B) FT-IR spectrum of 2,6-difluorobenzoic acid 150

Figure 4.21(A) FT-IR spectrum of complex **Cu-2-ClBZO** 151

Figure 4.21(B) FT-IR spectrum of 2-chlorobenzoic acid 151

Figure 4.22(A) FT-IR spectrum of complex **Cu-2-BrBZO** 152

Figure 4.22(B) FT-IR spectrum of 2-bromobenzoic acid 152

Figure 4.23(A) UV-Vis spectrum of complex **Cu-4-Cl-2-NO$_2$BZO** (6.00 x 10^{-3} mol L^{-1}; A = 697 nm, ε = 56 mol^{-1}Lcm^{-1}) 155

Figure 4.23(B) UV-Vis spectrum of complex **Cu-4-Cl-2-NO$_2$BZO** (1.20 x 10^{-5} mol L^{-1}; A = 319 nm, ε = 3600 mol^{-1}Lcm^{-1}; A = 262 nm, ε = 10 324 mol^{-1}Lcm^{-1}; A = 216 nm, ε = 30 129 mol^{-1}Lcm^{-1}) 155

Figure 4.24(A) UV-Vis spectrum of complex **Cu-2-Cl-4-NO$_2$BZO** (6.54 x 10^{-3} mol L^{-1}; A = 674 nm, ε = 63 mol^{-1}Lcm^{-1}) 156

Figure 4.24(B) UV-Vis spectrum of complex **Cu-2-Cl-4-NO$_2$BZO** (1.31 x 10^{-5} mol L^{-1}; A = 275 nm, ε = 24 477 mol^{-1}Lcm^{-1}; A = 211 nm, ε = 42 468 mol^{-1}Lcm^{-1}) 156

Figure 4.25(A) UV-Vis spectrum of complex **CuP-5-Cl-2-NO$_2$BZO** (5.90 x 10^{-3} mol L^{-1}; A = 662 nm, ε = 60 mol^{-1}Lcm^{-1}) 157

Figure 4.25(B) UV-Vis spectrum of complex **CuP-5-Cl-2-NO$_2$BZO** (1.18 x 10^{-5} mol L^{-1}; A = 274 nm, ε = 26 555 mol^{-1}Lcm^{-1}; A = 211 nm, ε = 43 376 mol^{-1}Lcm^{-1}) 157

LIST OF FIGURES

Page

Figure 4.26(A) UV-Vis spectrum of complex **Cu-2-Cl-6-FBZO** (6.33 x 10^{-3} mol L^{-1}; A = 735 nm, ε = 57 $mol^{-1}Lcm^{-1}$) 158

Figure 4.26(B) UV-Vis spectrum of complex **Cu-2-Cl-6-FBZO** (1.26 x 10^{-5} mol L^{-1};A = 264 nm, ε = 9920 $mol^{-1}Lcm^{-1}$; A = 212 nm, ε = 42 285 $mol^{-1}Lcm^{-1}$) 158

Figure 4.27(A) UV-Vis spectrum of complex **Cu-2-F-6-FBZO** (4.27 x 10^{-3} mol L^{-1}; A = 692 nm, ε = 69 $mol^{-1}Lcm^{-1}$) 159

Figure 4.27(B) UV-Vis spectrum of complex **Cu-2-F-6-FBZO** (4.27 x 10^{-6} mol L^{-1}; A = 264 nm, ε = 10 009 $mol^{-1}Lcm^{-1}$; A = 210 nm, ε = 45 380 $mol^{-1}Lcm^{-1}$) 159

Figure 4.28(A) UV-Vis spectrum of complex **Cu-2-ClBZO** (5.81 x 10^{-3} mol L^{-1}; A = 731 nm, ε = 65 $mol^{-1}Lcm^{-1}$) 160

Figure 4.28(B) UV-Vis spectrum of complex **Cu-2-ClBZO** (1.16 x 10^{-5} mol L^{-1}; A = 270 nm, ε = 9526 $mol^{-1}Lcm^{-1}$; A = 211 nm, ε = 47 783 $mol^{-1}Lcm^{-1}$) 160

Figure 4.29(A) UV-Vis spectrum of complex **Cu-2-BrBZO** (4.39 x 10^{-3} mol L^{-1}; A = 739 nm, ε = 55 $mol^{-1}Lcm^{-1}$) 161

Figure 4.29(B) UV-Vis spectrum of complex **Cu-2-BrBZO** (1.01 x 10^{-5} mol L^{-1}; A = 256 nm, ε = 16 300 $mol^{-1}Lcm^{-1}$; A = 211 nm, ε = 45 575 $mol^{-1}Lcm^{-1}$) 161

Figure 4.30 UV-Vis spectrum of $CuCl_2$ (0.022 mol L^{-1}; A = 758 nm, ε = 25 $mol^{-1}Lcm^{-1}$) 162

Figure 4.31 UV-Vis spectrum of $CuSO_4$ (0.022 mol L^{-1}; A = 768 nm, ε = 22 $mol^{-1}Lcm^{-1}$) 162

Figure 4.32(A) Cyclic voltammogram of complex **Cu-4-Cl-2-NO_2BZO**; Epa = anodic oxidation peak, Epc = cathodic reduction peak 165

Figure 4.32(B) Cyclic voltammogram of complex **Cu-2-Cl-4-NO_2BZO**; Epa = anodic oxidation peak, Epc = cathodic reduction peak 165

LIST OF FIGURES

Page

Figure 4.32(C) Cyclic voltammogram of complex **CuP-5-Cl-2-NO$_2$BZO**; Epa = anodic oxidation peak, Epc = cathodic reduction peak 166

Figure 4.32(D) Cyclic voltammogram of complex **Cu-2-Cl-6-FBZO**; Epa = anodic oxidation peak, Epc = cathodic reduction peak 166

Figure 4.32(E) Cyclic voltammogram of complex **Cu-2-F-6-FBZO**; Epa = anodic oxidation peak, Epc = cathodic reduction peak 167

Figure 4.32(F) Cyclic voltammogram of complex **Cu-2-ClBZO**; Epa = anodic oxidation peak, Epc = cathodic reduction peak 167

Figure 4.32(G) Cyclic voltammogram of complex **Cu-2-BrBZO**; Epa = anodic oxidation peak, Epc = cathodic reduction peak 168

Figure 4.33 Cleavage of supercoiled pBR322 by complex **Cu-4-Cl-2-NO$_2$BZO** at different concentrations in TN buffer pH 7.5. L1 Gene Ruler 1 kb DNA ladder, L2 DNA alone, L3 DNA + H_2O_2 alone, L4 DNA + 40 μM complex **Cu-4-Cl-2-NO$_2$BZO** alone (without H_2O_2). Lanes 5-12 DNA with increasing concentration of complex **Cu-4-Cl-2-NO$_2$BZO** + H_2O_2: lane 5, 5 μM; lane 6, 10 μM; lane 7, 15 μM; lane 8, 20 μM; lane 9, 25 μM; lane 10, 30 μM; lane 11, 35 μM; lane 12, 40 μM. 169

Figure 4.34 Cleavage of supercoiled pBR322 by complex **Cu-2-Cl-4-NO$_2$BZO** at different concentrations in TN buffer pH 7.5. L1 Gene Ruler 1 kb DNA ladder, L2 DNA alone, L3 DNA + H_2O_2 alone, L4 DNA + 40 μM complex **Cu-2-Cl-4-NO$_2$BZO** alone (without H_2O_2). Lanes 5-12 DNA with increasing concentration of complex **Cu-2-Cl-4-NO$_2$BZO** + H_2O_2: lane 5, 5 μM; lane 6, 10 μM; lane 7, 15 μM; lane 8, 20 μM; lane 9, 25 μM; lane 10, 30 μM; lane 11, 35 μM; lane 12, 40 μM. 170

Figure 4.35 Cleavage of supercoiled pBR322 by complex **CuP-5-Cl-2-NO$_2$BZO** at different concentrations in TN buffer pH 7.5. L1 Gene Ruler 1 kb DNA ladder, L2 DNA alone, L3 DNA + H_2O_2 alone, L4 DNA + 40 μM complex **CuP-5-Cl-2-NO$_2$BZO** alone (without H_2O_2). Lanes 5-12 DNA with increasing concentration of complex **CuP-5-Cl-2-NO$_2$BZO** + H_2O_2: lane 5, 5 μM; lane 6, 10 μM; lane 7, 15 μM; lane 8, 20 μM; lane 9, 25 μM; lane 10, 30 μM; lane 11, 35 μM; lane 12, 40 μM. 171

Figure 4.36 Cleavage of supercoiled pBR322 by complex **Cu-2-Cl-6-FBZO** at different concentrations in TN buffer pH 7.5. L1 Gene Ruler 1 kb DNA ladder, L2 DNA alone, L3 DNA + H_2O_2 alone, L4 DNA + 40 μM complex **Cu-2-Cl-6-FBZO** alone (without H_2O_2). Lanes 5-12 DNA with increasing concentration of complex **Cu-2-Cl-6-FBZO** + H_2O_2: lane 5, 5 μM; lane 6, 10 μM; lane 7, 15 μM; lane 8, 20 μM; lane 9, 25 μM; lane 10, 30 μM; lane 11, 35 μM; lane 12, 40 μM. 172

LIST OF FIGURES

Page

Figure 4.37 Cleavage of supercoiled pBR322 by complex **Cu-2-F-6-FBZO** at different concentrations in TN buffer pH 7.5. L1 Gene Ruler 1 kb DNA ladder, L2 DNA alone, L3 DNA + H_2O_2 alone, L4 DNA + 40 μM complex **Cu-2-F-6-FBZO** alone (without H_2O_2). Lanes 5-12 DNA with increasing concentration of complex **Cu-2-F-6-FBZO** + H_2O_2: lane 5, 5 μM; lane 6, 10 μM; lane 7, 15 μM; lane 8, 20 μM; lane 9, 25 μM; lane 10, 30 μM; lane 11, 35 μM; lane 12, 40 μM. 173

Figure 4.38 Cleavage of supercoiled pBR322 by complex **Cu-2-ClBZO** at different concentrations in TN buffer pH 7.5. L1 Gene Ruler 1 kb DNA ladder, L2 DNA alone, L3 DNA + H_2O_2 alone, L4 DNA + 40 μM complex **Cu-2-ClBZO** alone (without H_2O_2). Lanes 5-12 DNA with increasing concentration of complex **Cu-2-ClBZO** + H_2O_2: lane 5, 5 μM; lane 6, 10 μM; lane 7, 15 μM; lane 8, 20 μM; lane 9, 25 μM; lane 10, 30 μM; lane 11, 35 μM; lane 12, 40 μM. 174

Figure 4.39 Cleavage of supercoiled pBR322 by complex **Cu-2-BrBZO** at different concentrations in TN buffer pH 7.5. L1 Gene Ruler 1 kb DNA ladder, L2 DNA alone, L3 DNA + H_2O_2 alone, L4 DNA + 40 μM complex **Cu-2-BrBZO** alone (without H_2O_2). Lanes 5-12 DNA with increasing concentration of complex **Cu-2-BrBZO** + H_2O_2: lane 5, 5 μM; lane 6, 10 μM; lane 7, 15 μM; lane 8, 20 μM; lane 9, 25 μM; lane 10, 30 μM; lane 11, 35 μM; lane 12, 40 μM. 175

Figure 4.40 Cleavage of supercoiled pBR322 by $CuCl_2$ at different concentrations in TN buffer pH 7.5. L1 Gene Ruler 1 kb DNA ladder, L2 DNA alone, L3 DNA + H_2O_2 alone, L4 DNA + 40 μM $CuCl_2$ alone (without H_2O_2). Lanes 5-12 DNA with increasing concentration of $CuCl_2$ + H_2O_2: lane 5, 5 μM; lane 6, 10 μM; lane 7, 15 μM; lane 8, 20 μM; lane 9, 25 μM; lane 10, 30 μM; lane 11, 35 μM; lane 12, 40 μM. 177

Figure 4.41 Cleavage of supercoiled pBR322 by $CuSO_4$ at different concentrations in TN buffer pH 7.5. L1 Gene Ruler 1 kb DNA ladder, L2 DNA alone, L3 DNA + H_2O_2 alone, L4 DNA + 40 μM $CuSO_4$ alone (without H_2O_2). Lanes 5-12 DNA with increasing concentration of $CuSO_4$ + H_2O_2: lane 5, 5 μM; lane 6, 10 μM; lane 7, 15 μM; lane 8, 20 μM; lane 9, 25 μM; lane 10, 30 μM; lane 11, 35 μM; lane 12, 40 μM. 178

Figure 4.42 Effect of various scavengers on the cleavage of pBR322 by 40 μM complex **Cu-4-Cl-2-NO$_2$BZO** Lane 1, Gene Ruler 1 kb DNA ladder; lane 2, DNA alone; lane 3, DNA + 40 μM of complex **Cu-4-Cl-2-NO$_2$BZO** + H_2O_2. Lanes 4 – 12 involves reaction of 40 μM complex **Cu-4-Cl-2-NO$_2$BZO** + H_2O_2 with DNA in presence of various scavengers; lane 4, t-butyl alcohol (1 M); lane 5, 1 mM Mannitol; lane 6, DMSO (1 M); lane 7, 1 mM NaN_3; lane 8, 10 mM NaN_3; lane 9, 20 mM NaN_3; lane 10, 30 mM NaN_3; lane 11, 40 mM NaN_3; lane 12, 50 mM NaN_3. 180

LIST OF FIGURES

		Page
Figure 4.43	Effect of various scavengers on the cleavage of pBR322 by 40 µM complex **Cu-2-Cl-4-NO$_2$BZO** Lane 1, Gene Ruler 1 kb DNA ladder; lane 2, DNA alone; lane 3, DNA + 40 µM of complex **Cu-2-Cl-4-NO$_2$BZO** + H_2O_2. Lanes 4 – 12 involves reaction of 40 µM complex **Cu-2-Cl-4-NO$_2$BZO** + H_2O_2 with DNA in presence of various scavengers; lane 4, t-butyl alcohol (1 M); lane 5, 1 mM Mannitol; lane 6, DMSO (1 M); lane 7, 1 mM NaN_3; lane 8, 10 mM NaN_3; lane 9, 20 mM NaN_3; lane 10, 30 mM NaN_3; lane 11, 40 mM NaN_3; lane 12, 50 mM NaN_3.	180
Figure 4.44	Effect of various scavengers on the cleavage of pBR322 by 40 µM complex **CuP-5-Cl-2-NO$_2$BZO** Lane 1, Gene Ruler 1 kb DNA ladder; lane 2, DNA alone; lane 3, DNA + 40 µM of complex **CuP-5-Cl-2-NO$_2$BZO** + H_2O_2. Lanes 4 – 12 involves reaction of 40 µM complex **CuP-5-Cl-2-NO$_2$BZO** + H_2O_2 with DNA in presence of various scavengers; lane 4, t-butyl alcohol (1 M); lane 5, 1 mM Mannitol; lane 6, DMSO (1 M); lane 7, 1 mM NaN_3; lane 8, 10 mM NaN_3; lane 9, 20 mM NaN_3; lane 10, 30 mM NaN_3; lane 11, 40 mM NaN_3; lane 12, 50 mM NaN_3.	181
Figure 4.45	Effect of various scavengers on the cleavage of pBR322 by 40 µM complex **Cu-2-Cl-6-FBZO** Lane 1, Gene Ruler 1 kb DNA ladder; lane 2, DNA alone; lane 3, DNA + 40 µM of complex **Cu-2-Cl-6-FBZO** + H_2O_2. Lanes 4 – 12 involves reaction of 40 µM complex **Cu-2-Cl-6-FBZO** + H_2O_2 with DNA in presence of various scavengers; lane 4, t-butyl alcohol (1 M); lane 5, 1 mM Mannitol; lane 6, DMSO (1 M); lane 7, 1 mM NaN_3; lane 8, 10 mM NaN_3; lane 9, 20 mM NaN_3; lane 10, 30 mM NaN_3; lane 11, 40 mM NaN_3; lane 12, 50 mM NaN_3.	181
Figure 4.46	Effect of various scavengers on the cleavage of pBR322 by 40 µM complex **Cu-2-F-6-FBZO** Lane 1, Gene Ruler 1 kb DNA ladder; lane 2, DNA alone; lane 3, DNA + 40 µM of complex **Cu-2-F-6-FBZO** + H_2O_2. Lanes 4 – 12 involves reaction of 40 µM complex **Cu-2-F-6-FBZO** + H_2O_2 with DNA in presence of various scavengers; lane 4, t-butyl alcohol (1 M); lane 5, 1 mM Mannitol; lane 6, DMSO (1 M); lane 7, 1 mM NaN_3; lane 8, 10 mM NaN_3; lane 9, 20 mM NaN_3; lane 10, 30 mM NaN_3; lane 11, 40 mM NaN_3; lane 12, 50 mM NaN_3.	182
Figure 4.47	Effect of various scavengers on the cleavage of pBR322 by 40 µM complex **Cu-2-ClBZO** Lane 1, Gene Ruler 1 kb DNA ladder; lane 2, DNA alone; lane 3, DNA + 40 µM of complex **Cu-2-ClBZO** + H_2O_2. Lanes 4 – 12 involves reaction of 40 µM complex **Cu-2-ClBZO** + H_2O_2 with DNA in presence of various scavengers; lane 4, t-butyl alcohol (1 M); lane 5, 1 mM Mannitol; lane 6, DMSO (1 M); lane 7, 1 mM NaN_3; lane 8, 10 mM NaN_3; lane 9, 20 mM NaN_3; lane 10, 30 mM NaN_3; lane 11, 40 mM NaN_3; lane 12, 50 mM NaN_3.	182

LIST OF FIGURES

Page

Figure 4.48 Effect of various scavengers on the cleavage of pBR322 by 40 μM complex **Cu-2-BrBZO** Lane 1, Gene Ruler 1 kb DNA ladder; lane 2, DNA alone; lane 3, DNA + 40 μM of complex **Cu-2-BrBZO** + H_2O_2. Lanes 4 – 12 involves reaction of 40 μM complex **Cu-2-BrBZO** + H_2O_2 with DNA in presence of various scavengers; lane 4, t-butyl alcohol (1 M); lane 5, 1 mM Mannitol; lane 6, DMSO (1 M); lane 7, 1 mM NaN_3, lane 8, 10 mM NaN_3, lane 9, 20 mM NaN_3, lane 10, 30 mM NaN_3, lane 11, 40 mM NaN_3, lane 12, 50 mM NaN_3. 183

Figure 4.49 The proposed DNA cleavage mechanism of complexes **Cu-4-Cl-2-NO_2BZO**, **Cu-2-Cl-4-NO_2BZO**, **CuP-5-Cl-2-NO_2BZO**, **Cu-2-Cl-6-FBZO**, **Cu-2-F-6-FBZO**, **Cu-2-ClBZO** and **Cu-2-BrBZO** in the presence of H_2O_2 183

Figure 5.1 The partial polymeric structure of complex **MnP-4-Cl-2-NO_2BZO**, showing 50 % probability displacement ellipsoids and the atomic numbering 195

Figure 5.2 The crystal packing of polymeric complex **MnP-4-Cl-2-NO_2BZO** 196

Figure 5.3 The partial polymeric structure of complex **MnP-3-NO_2-5-NO_2BZO**, showing 50 % probability displacement ellipsoids and the atomic numbering 198

Figure 5.4 The crystal packing of polymeric complex **MnP-3-NO_2-5-NO_2BZO** 198

Figure 5.5 The molecular structure of complex **Mn-4-NO_2BZO**, showing 50 % probability displacement ellipsoids and the atomic numbering 200

Figure 5.6 The crystal packing of complex **Mn-4-NO_2BZO** 201

Figure 5.7 The partial polymeric structure of complex **MnP-4-NH_2BZO**, showing 50 % probability displacement ellipsoids and the atomic numbering 205

Figure 5.8 The crystal packing of polymeric complex **MnP-4-NH_2BZO** 206

Figure 5.9 The partial polymeric structure of complex **MnP-4-FBZO**, showing 50 % probability displacement ellipsoids and the atomic numbering 210

LIST OF FIGURES

Page

Figure 5.10 The crystal packing of polymeric complex **MnP-4-FBZO** 211

Figure 5.11 The partial polymeric structure of complex **MnPGLY**, showing 50 % probability displacement ellipsoids and the atomic numbering 215

Figure 5.12 The crystal packing of polymeric complex **MnPGLY** 216

Figure 5.13 FT-IR spectrum of complex **MnP-4-Cl-2-NO$_2$BZO** 224

Figure 5.14(A) FT-IR spectrum of complex **MnP-3-NO$_2$-5-NO$_2$BZO** 224

Figure 5.14(B) FT-IR spectrum of 3,5-dinitrobenzoic acid 225

Figure 5.15(A) FT-IR spectrum of complex **Mn-4-NO$_2$BZO** 225

Figure 5.15(B) FT-IR spectrum of 4-nitrobenzoic acid 226

Figure 5.16(A) FT-IR spectrum of complex **MnP-4-NH$_2$BZO** 226

Figure 5.16(B) FT-IR spectrum of 4-aminobenzoic acid 227

Figure 5.17(A) FT-IR spectrum of complex **MnP-4-FBZO** 227

Figure 5.17(B) FT-IR spectrum of 4-flourobenzoic acid 228

Figure 5.18 Postulated structure of partial polymeric complex **MnP-4-ClBZO** 228

Figure 5.19(A) FT-IR spectrum of complex **MnP-4-ClBZO** 229

Figure 5.19(B) FT-IR spectrum of 4-chlorobenzoic acid 229

Figure 5.20 FT-IR spectrum of complex **MnPGLY** 230

Figure 5.21 Chemical structure of complex **MnPyr** [73] 230

Figure 5.22 FT-IR spectrum of complex **MnPyr** 231

LIST OF FIGURES

Page

Figure 5.23(A) UV-Vis spectrum of complex **MnP-4-Cl-2-NO_2BZO** (8.37×10^{-3} mol L^{-1}) 234

Figure 5.23(B) UV-Vis spectrum of complex **MnP-4-Cl-2-NO_2BZO** (2.00×10^{-5} mol L^{-1}; A = 318 nm, $\varepsilon = 4127$ $mol^{-1}Lcm^{-1}$; A = 262 nm, $\varepsilon = 11122$ $mol^{-1}Lcm^{-1}$; A = 214 nm, $\varepsilon = 41036$ $mol^{-1}Lcm^{-1}$) 234

Figure 5.24(A) UV-Vis spectrum of complex **MnP-3-NO_2-5-NO_2BZO** (5.22×10^{-3} mol L^{-1}) 235

Figure 5.24(B) UV-Vis spectrum of complex **MnP-3-NO_2-5-NO_2BZO** (2.08×10^{-5} mol L^{-1}; A = 238 nm, $\varepsilon = 32169$ $mol^{-1}Lcm^{-1}$; A = 212 nm, $\varepsilon = 45175$ $mol^{-1}Lcm^{-1}$) 235

Figure 5.25(A) UV-Vis spectrum of complex **Mn-4-NO_2BZO** (6.45×10^{-3} mol L^{-1}) 236

Figure 5.25(B) UV-Vis spectrum of complex **Mn-4-NO_2BZO** (2.57×10^{-5} mol L^{-1}; A = 273 nm, $\varepsilon = 19411$ $mol^{-1}Lcm^{-1}$; A = 210 nm, $\varepsilon = 18785$ $mol^{-1}Lcm^{-1}$) 236

Figure 5.26(A) UV-Vis spectrum of complex **MnP-4-NH_2BZO** (0.010 mol L^{-1}) 237

Figure 5.26(B) UV-Vis spectrum of complex **MnP-4-NH_2BZO** (8.23×10^{-6} mol L^{-1}; A = 265 nm, $\varepsilon = 30469$ $mol^{-1}Lcm^{-1}$; A = 210 nm, $\varepsilon = 36701$ $mol^{-1}Lcm^{-1}$) 237

Figure 5.27(A) UV-Vis spectrum of complex **MnP-4-FBZO** (6.26×10^{-3} mol L^{-1}) 238

Figure 5.27(B) UV-Vis spectrum of complex **MnP-4-FBZO** (2.50×10^{-5} mol L^{-1}; A = 223 nm, $\varepsilon = 18\ 000$ $mol^{-1}Lcm^{-1}$) 238

Figure 5.28(A) UV-Vis spectrum of complex **MnP-4-ClBZO** (5.82×10^{-3} mol L^{-1}) 239

Figure 5.28(B) UV-Vis spectrum of complex **MnP-4-ClBZO** (2.32×10^{-5} mol L^{-1}; A = 225 nm, $\varepsilon = 17\ 835$ $mol^{-1}Lcm^{-1}$) 239

LIST OF FIGURES

		Page
Figure 5.29(A)	UV-Vis spectrum of complex **MnPGLY** (0.015 mol L^{-1})	240
Figure 5.29(B)	UV-Vis spectrum of complex **MnPGLY** (3.05 x 10^{-3} mol L^{-1}; A = 212 nm, ε = 156 $mol^{-1}Lcm^{-1}$)	240
Figure 5.30(A)	UV-Vis spectrum of complex **MnPyr** (0.012 mol L^{-1})	241
Figure 5.30(B)	UV-Vis spectrum of complex **MnPyr** (4.65 x 10^{-5} mol L^{-1}; A = 262 nm, ε = 8699 $mol^{-1}Lcm^{-1}$; A = 213 nm, ε = 18147 $mol^{-1}Lcm^{-1}$)	241
Figure 5.31	UV-Vis spectrum of complex $MnCl_2$ (0.031 mol L^{-1}; A = 211 nm; ε = 11 $mol^{-1}Lcm^{-1}$)	242
Figure 5.32(A)	Cyclic voltammogram of complex **MnP-4-Cl-2-NO$_2$BZO**; Epa = anodic oxidation peak, Epc = cathodic reduction peak	245
Figure 5.32(B)	Cyclic voltammogram of complex **MnP-3-NO$_2$-5-NO$_2$BZO**; Epa = anodic oxidation peak, Epc = cathodic reduction peak	245
Figure 5.32(C)	Cyclic voltammogram of complex **Mn-4-NO$_2$BZO**; Epa = anodic oxidation peak, Epc = cathodic reduction peak	246
Figure 5.32(D)	Cyclic voltammogram of complex **MnP-4-NH$_2$BZO**; Epa = anodic oxidation peak, Epc = cathodic reduction peak	246
Figure 5.32(E)	Cyclic voltammogram of complex **MnP-4-FBZO**; Epa = anodic oxidation peak, Epc = cathodic reduction peak	247
Figure 5.32(F)	Cyclic voltammogram of complex **MnP-4-ClBZO**; Epa = anodic oxidation peak, Epc = cathodic reduction peak	247
Figure 5.32(G)	Cyclic voltammogram of complex **MnPGLY**; Epa = anodic oxidation peak, Epc = cathodic reduction peak	248
Figure 5.32(H)	Cyclic voltammogram of complex **MnPyr**; Epa = anodic oxidation peak, Epc = cathodic reduction peak	248

LIST OF FIGURES

Page

Figure 5.33 Cleavage of supercoiled pBR322 by complex **MnP-4-Cl-2-NO$_2$BZO** at different concentrations in TN buffer pH 7.5. L1 Gene Ruler 1 kb DNA ladder; L2, DNA alone; L3, DNA + H_2O_2 alone; L4, DNA + complex alone (80 µM). Lanes 5-12 DNA with increasing concentration of complex **MnP-4-Cl-2-NO$_2$BZO** + H_2O_2: lane 5, 10 µM; lane 6, 20 µM; lane 7, 30 µM; lane 8, 40 µM; lane 9, 50 µM; lane 10, 60 µM; lane 11, 70 µM; lane 12, 80 µM. 250

Figure 5.34 Cleavage of supercoiled pBR322 by complex **MnP-3-NO$_2$-5-NO$_2$BZO** at different concentrations in TN buffer pH 7.5. L1 Gene Ruler 1 kb DNA ladder; L2, DNA alone; L3, DNA + H_2O_2 alone; L4, DNA + complex alone (160 µM). Lanes 5-12 DNA with increasing concentration of complex **MnP-3-NO$_2$-5-NO$_2$BZO** + H_2O_2: lane 5, 80 µM; lane 6, 100 µM; lane 7, 110 µM; lane 8, 120 µM; lane 9, 130 µM; lane 10, 140 µM; lane 11, 150 µM; lane 12, 160 µM. 251

Figure 5.35 Cleavage of supercoiled pBR322 by complex **Mn-4-NO$_2$BZO** at different concentrations in TN buffer pH 7.5. L1 Gene Ruler 1 kb DNA ladder; L2, DNA alone; L3, DNA + H_2O_2 alone; L4, DNA + complex alone (160 µM). Lanes 5-12 DNA with increasing concentration of complex **Mn-4-NO$_2$BZO** + H_2O_2: lane 5, 80 µM; lane 6, 100 µM; lane 7, 110 µM; lane 8, 120 µM; lane 9, 130 µM; lane 10, 140 µM; lane 11, 150 µM; lane 12, 160 µM. 252

Figure 5.36 Cleavage of supercoiled pBR322 by complex **MnP-4-NH$_2$BZO** at different concentrations in TN buffer pH 7.5. L1 Gene Ruler 1 kb DNA ladder; L2, DNA alone; L3, DNA + H_2O_2 alone; L4, DNA + complex alone (160 µM). Lanes 5-12 DNA with increasing concentration of complex **MnP-4-NH$_2$BZO** + H_2O_2: lane 5, 80 µM; lane 6, 100 µM; lane 7, 110 µM; lane 8, 120 µM; lane 9, 130 µM; lane 10, 140 µM; lane 11, 150 µM; lane 12, 160 µM. 253

Figure 5.37 Cleavage of supercoiled pBR322 by complex **MnP-4-FBZO** at different concentrations in TN buffer pH 7.5. L1 Gene Ruler 1 kb DNA ladder; L2, DNA alone; L3, DNA + H_2O_2 alone; L4 DNA + complex alone (80 µM). Lanes 5-12 DNA with increasing concentration of complex **MnP-4-FBZO** + H_2O_2: lane 5, 10 µM; lane 6, 20 µM; lane 7, 30 µM; lane 8, 40 µM; lane 9, 50 µM; lane 10, 60 µM; lane 11, 70 µM; lane 12, 80 µM. 254

Figure 5.38 Cleavage of supercoiled pBR322 by complex **MnP-4-ClBZO** at different concentrations in TN buffer pH 7.5. L1 Gene Ruler 1 kb DNA ladder; L2, DNA alone; L3, DNA + H_2O_2 alone; L4 DNA + complex alone (80 µM). Lanes 5-12 DNA with increasing concentration of complex **MnP-4-ClBZO** + H_2O_2: lane 5, 10 µM; lane 6, 20 µM; lane 7, 30 µM; lane 8, 40 µM; lane 9, 50 µM; lane 10, 60 µM; lane 11, 70 µM; lane 12, 80 µM. 255

LIST OF FIGURES

Page

Figure 5.39 Cleavage of supercoiled pBR322 by complex **MnPGLY** at different concentrations in TN buffer pH 7.5. L1 Gene Ruler 1 kb DNA ladder; L2, DNA alone; L3, DNA + H_2O_2 alone; L4, DNA + complex alone (80 μM). Lanes 5-12 DNA with increasing concentration of complex **MnPGLY** + H_2O_2: lane 5, 10 μM; lane 6, 20 μM; lane 7, 30 μM; lane 8, 40 μM; lane 9, 50 μM; lane 10, 60 μM; lane 11, 70 μM; lane 12, 80 μM. 256

Figure 5.40 Cleavage of supercoiled pBR322 by complex **MnPyr** at different concentrations in TN buffer pH 7.5. L1 Gene Ruler 1 kb DNA ladder; L2, DNA alone; L3, DNA + H_2O_2 alone; L4, DNA + complex alone (80 μM). Lanes 5-12 DNA with increasing concentration of complex **MnPyr** + H_2O_2: lane 5, 10 μM; lane 6, 20 μM; lane 7, 30 μM; lane 8, 40 μM; lane 9, 50 μM; lane 10, 60 μM; lane 11, 70 μM; lane 12, 80 μM. 257

Figure 5.41 Cleavage of supercoiled pBR322 by $MnCl_2$ at different concentrations in TN buffer pH 7.5. L1 Gene Ruler 1 kb DNA ladder; L2, DNA alone; L3, DNA + H_2O_2 alone; L4, DNA + $MnCl_2$ alone (160 μM); lane 5, 80 μM; lane 6, 100 μM; lane 7, 110 μM; lane 8, 120 μM; lane 9, 130 μM; lane 10, 140 μM; lane 11, 150 μM; lane 12, 160 μM 259

Figure 5.42 Effect of various scavengers on the cleavage of pBR322 by 50 μM complex **MnP-4-Cl-2-NO$_2$BZO**. Lane 1, Gene Ruler 1 kb DNA ladder; lane 2, DNA alone; lane 3, DNA + 50 μM complex **MnP-4-Cl-2-NO$_2$BZO** + H_2O_2. Lanes 4 – 12 involves reaction of 50 μM complex **MnP-4-Cl-2-NO$_2$BZO** + H_2O_2 with DNA in presence of various scavengers; lane 4, t-butyl alcohol (1 M); lane 5, 1 mM Mannitol; lane 6, DMSO (1 M); lane 7, 1 mM NaN_3; lane 8, 10 mM NaN_3; lane 9, 20 mM NaN_3; lane 10, 30 mM NaN_3; lane 11, 50 mM NaN_3; lane 12, 100 mM NaN_3. 261

Figure 5.43 Effect of various scavengers on the cleavage of pBR322 by 100 μM complex **MnP-3-NO$_2$-5-NO$_2$BZO**. Lane 1, Gene Ruler 1 kb DNA ladder; lane 2, DNA alone; lane 3, DNA + 100 μM complex **MnP-3-NO$_2$-5-NO$_2$BZO** + H_2O_2. Lanes 4 – 12 involves reaction of 100 μM complex **MnP-3-NO$_2$-5-NO$_2$BZO** + H_2O_2 with DNA in presence of various scavengers; lane 4, t-butyl alcohol (1 M); lane 5, 1 mM Mannitol; lane 6, DMSO (1 M); lane 7, 1 mM NaN_3; lane 8, 10 mM NaN_3; lane 9, 20 mM NaN_3; lane 10, 30 mM NaN_3; lane 11, 50 mM NaN_3; lane 12, 100 mM NaN_3. 261

Figure 5.44 Effect of various scavengers on the cleavage of pBR322 by 110 μM complex **Mn-4-NO$_2$BZO**. Lane 1, Gene Ruler 1 kb DNA ladder; lane 2, DNA alone; lane 3, DNA + 110 μM complex **Mn-4-NO$_2$BZO** + H_2O_2. Lanes 4 – 12 involves reaction of 110 μM complex **Mn-4-NO$_2$BZO** + H_2O_2 with DNA in presence of various scavengers; lane 4, t-butyl alcohol (1 M); lane 5, 1 mM Mannitol; lane 6, DMSO (1 M); lane 7, 1 mM NaN_3; lane 8, 10 mM NaN_3; lane 9, 20 mM NaN_3; lane 10, 30 mM NaN_3; lane 11, 50 mM NaN_3; lane 12, 100 mM NaN_3. 262

LIST OF FIGURES

Page

Figure 5.45 Effect of various scavengers on the cleavage of pBR322 by 100 μM complex **MnP-4-NH$_2$BZO**. Lane 1, Gene Ruler 1 kb DNA ladder; lane 2, DNA alone; lane 3, DNA + 100 μM complex **MnP-4-NH$_2$BZO** + H_2O_2. Lanes 4 – 12 involves reaction of 100 μM complex **MnP-4-NH$_2$BZO** + H_2O_2 with DNA in presence of various scavengers; lane 4, t-butyl alcohol (1 M); lane 5, 1 mM Mannitol; lane 6, DMSO (1 M); lane 7, 1 mM NaN_3; lane 8, 10 mM NaN_3; lane 9, 20 mM NaN_3; lane 10, 30 mM NaN_3; lane 11, 50 mM NaN_3; lane 12, 100 mM NaN_3. 262

Figure 5.46 Effect of various scavengers on the cleavage of pBR322 by 50 μM complex **MnP-4-FBZO**. Lane 1, Gene Ruler 1 kb DNA ladder; lane 2, DNA alone; lane 3, DNA + 50 μM complex **MnP-4-FBZO** + H_2O_2. Lanes 4 – 12 involves reaction of 50 μM complex **MnP-4-FBZO** + H_2O_2 with DNA in presence of various scavengers; lane 4, t-butyl alcohol (1 M); lane 5, 1 mM Mannitol; lane 6, DMSO (1 M); lane 7, 1 mM NaN_3; lane 8, 10 mM NaN_3; lane 9, 20 mM NaN_3; lane 10, 30 mM NaN_3; lane 11, 50 mM NaN_3; lane 12, 100 mM NaN_3. 263

Figure 5.47 Effect of various scavengers on the cleavage of pBR322 by 60 μM complex **MnP-4-ClBZO**. Lane 1, Gene Ruler 1 kb DNA ladder; lane 2, DNA alone; lane 3, DNA + 60 μM complex **MnP-4-ClBZO** + H_2O_2. Lanes 4 – 12 involves reaction of 60 μM complex **MnP-4-ClBZO** + H_2O_2 with DNA in presence of various scavengers; lane 4, t-butyl alcohol (1 M); lane 5, 1 mM Mannitol; lane 6, DMSO (1 M); lane 7, 1 mM NaN_3; lane 8, 10 mM NaN_3; lane 9, 20 mM NaN_3; lane 10, 30 mM NaN_3; lane 11, 50 mM NaN_3; lane 12, 100 mM NaN_3. 263

Figure 5.48 Effect of various scavengers on the cleavage of pBR322 by 60 μM complex **MnPGLY**. Lane 1, Gene Ruler 1 kb DNA ladder; lane 2, DNA alone; lane 3, DNA + 60 μM complex **MnPGLY** + H_2O_2. Lanes 4 – 12 involves reaction of 60 μM complex **MnPGLY** + H_2O_2 with DNA in presence of various scavengers; lane 4, t-butyl alcohol (1 M); lane 5, 1 mM Mannitol; lane 6, DMSO (1 M); lane 7, 1 mM NaN_3; lane 8, 10 mM NaN_3; lane 9, 20 mM NaN_3; lane 10, 30 mM NaN_3; lane 11, 50 mM NaN_3; lane 12, 100 mM NaN_3. 264

Figure 5.49 Effect of various scavengers on the cleavage of pBR322 by 60 μM complex **MnPyr**. Lane 1, Gene Ruler 1 kb DNA ladder; lane 2, DNA alone; lane 3, DNA + 60 μM complex **MnPyr** + H_2O_2. Lanes 4 – 12 involves reaction of 60 μM complex **MnPyr** + H_2O_2 with DNA in presence of various scavengers; lane 4, t-butyl alcohol (1 M); lane 5, 1 mM Mannitol; lane 6, DMSO (1 M); lane 7, 1 mM NaN_3; lane 8, 10 mM NaN_3; lane 9, 20 mM NaN_3; lane 10, 30 mM NaN_3; lane 11, 50 mM NaN_3; lane 12, 100 mM NaN_3. 264

Figure 5.50 The proposed DNA cleavage mechanism of complexes **MnP-4-Cl-2-NO$_2$BZO**, **MnP-3-NO$_2$-5-NO$_2$BZO**, **Mn-4-NO$_2$BZO**, **MnP-4-NH$_2$BZO**, **MnP-4-FBZO**, **MnP-4-ClBZO**, **MnPGLY** and **MnPyr** 265

LIST OF FIGURES

		Page
Figure 6.1	The postulated chemical structure of complexes **VOPhen**, **VODMPhen**, **VODPPhen** and **VODMPPhen**	271
Figure 6.2(A)	FT-IR spectrum of complex **VOPhen**	274
Figure 6.2(B)	FT-IR spectrum of 1,10-phenanthroline	274
Figure 6.3(A)	FT-IR spectrum of complex **VODMPhen**	275
Figure 6.3(B)	FT-IR spectrum of 2,9-dimethly-1,10-phenanthroline	275
Figure 6.4(A)	FT-IR spectrum of complex **VODPPhen**	276
Figure 6.4(B)	FT-IR spectrum of 4,7-diphenyl-1,10-phenanthroline	276
Figure 6.5(A)	FT-IR spectrum of complex **VODMPPhen**	277
Figure 6.5(B)	FT-IR spectrum of 2,9-dimethly-4,7-diphenyl-1,10-phenanthroline	277
Figure 6.6	Absorption spectra of complex **VOPhen** in the absence and in the presence of increasing amount of DNA, [complex] = 20 μM, [DNA] = 20-120 μM	281
Figure 6.7	Absorption spectra of complex **VODMPhen** in the absence and in the presence of increasing amount of DNA, [complex] = 20 μM, [DNA] = 20-120 μM	281
Figure 6.8	Absorption spectra of complex **VODPPhen** in the absence and in the presence of increasing amount of DNA, [complex] = 20 μM, [DNA] = 10-60 μM	282
Figure 6.9	Absorption spectra of complex **VODMPPhen** in the absence and in the presence of increasing amount of DNA, [complex] = 20 μM, [DNA] = 10-60 μM	282
Figure 6.10	Plot of [DNA]/(ε_a- ε_f) versus [DNA] of complex **VOPhen**	283
Figure 6.11	Plot of [DNA]/(ε_a- ε_f) versus [DNA] of complex **VODMPhen**	283
Figure 6.12	Plot of [DNA]/(ε_a- ε_f) versus [DNA] of complex **VODPPhen**	284

LIST OF FIGURES

Page

Figure 6.13	Plot of [DNA]/(ε_a- ε_f) versus [DNA] of complex **VODMPPhen**	284
Figure 6.14	Absorption spectra of complex **VO_2PP** in the absence and in the presence of increasing amount of DNA, [complex] = 40 µM, [DNA] = 120 µM (Ratio DNA: Complex; 1:3)	287
Figure 6.15	Absorption spectra of complex **Cu-2-Cl-6-FBZO** in the absence and in the presence of increasing amount of DNA, [complex] = 13 µM, [DNA] = 39 µM (Ratio DNA: Complex; 1:3)	287
Figure 6.16	Absorption spectra of complex **Mn-4-NO_2BZO** in the absence and in the presence of increasing amount of DNA, [complex] = 26 µM, [DNA] = 78 µM (Ratio DNA: Complex; 1:3)	288
Figure 6.17	Effect of increasing amounts of complexes **VOPhen**, **VODMPhen**, **VODPPhen** and **VODMPPhen** on the relative viscosities of CT-DNA at 30 (± 0.1) °C, [DNA] = 200 µM	289
Figure 6.18	(a) CD spectrum of CT DNA in the absence of complex (50 µM); (b) CD spectrum of CT DNA (50 µM) in the presence of complex **VOPhen** (50µM); (c) CD spectrum of CT DNA (50 µM) in the presence of complex **VODMPhen** (50µM)	291
Figure 6.19	Cleavage of supercoiled pBR322 by complex **VOPhen** at different concentrations in Tris-HCl buffer pH 7.5. L1 Gene Ruler 1 kb DNA ladder, L2 DNA alone, L3 H_2O_2 alone, L4 complex **VOPhen** alone (40 µM). Lanes 5-12 DNA with increasing concentration of complex **VOPhen** + H_2O_2: lane 5, 5 µM; lane 6, 10 µM; lane 7, 15 µM; lane 8, 20 µM; lane 9, 25 µM; lane 10, 30 µM; lane 11, 35 µM; lane 12, 40 µM.	294
Figure 6.20	Cleavage of supercoiled pBR322 by complex **VOPhen** at different concentrations in Tris-HCl buffer pH 7.5. L1 Gene Ruler 1 kb DNA ladder, L2 DNA alone, Lanes 3-12 DNA with increasing concentration of complex **VOPhen**: lane 3, 50 µM; lane 4, 70 µM; lane 5, 100 µM; lane 6, 120 µM; lane 7, 140 µM; lane 8, 160 µM; lane 9, 180 µM; lane 10, 200 µM; lane 11, 220 µM; lane 12, 240 µM.	294
Figure 6.21	Cleavage of supercoiled pBR322 by complex **VODMPhen** at different concentrations in Tris-HCl buffer pH 7.5. L1 Gene Ruler 1 kb DNA ladder, L2 DNA alone, L3 H_2O_2 alone, L4 complex **VODMPhen** alone (240 µM). Lanes 5-12 DNA with increasing concentration of complex **VODMPhen** + H_2O_2: lane 5, 100 µM; lane 6, 120 µM; lane 7, 140 µM; lane 8, 160 µM; lane 9, 180 µM; lane 10, 200 µM; lane 11, 220 µM; lane 12, 240 µM.	295

LIST OF FIGURES

		Page
Figure 6.22	Cleavage of supercoiled pBR322 by complex **VODPPhen** at different concentrations in Tris-HCl buffer pH 7.5. L1 Gene Ruler 1 kb DNA ladder, L2 DNA alone, L3 H_2O_2 alone, L4 complex **VODPPhen** alone (40 μM). Lanes 5-12 DNA with increasing concentration of complex **VODPPhen** + H_2O_2: lane 5, 5 μM; lane 6, 10 μM; lane 7, 15 μM; lane 8, 20 μM; lane 9, 25 μM; lane 10, 30 μM; lane 11, 35 μM; lane 12, 40 μM.	295
Figure 6.23	Cleavage of supercoiled pBR322 by complex **VODMPPhen** at different concentrations in Tris-HCl buffer pH 7.5. L1 Gene Ruler 1 kb DNA ladder, L2 DNA alone, L3 H_2O_2 alone, L4 complex **VODMPPhen** alone (240 μM). Lanes 5-12 DNA with increasing concentration of complex **VODMPPhen** + H_2O_2: lane 5, 100 μM; lane 6, 120 μM; lane 7, 140 μM; lane 8, 160 μM; lane 9, 180 μM; lane 10, 200 μM; lane 11, 220 μM; lane 12, 240 μM.	296
Figure 6.24	Effect of various scavengers on the cleavage of pBR322 by 25 μM complex **VOPhen**. Lane 1, Gene Ruler 1 kb DNA ladder; Lane 2, DNA alone; Lane 3, DNA + 25 μM complex **VOPhen** + H_2O_2. Lanes 4 – 12 involves reaction of 25 μM complex **VOPhen** + H_2O_2 with DNA in presence of various scavengers; lane 4, t-butyl alcohol (1 M); lane 5, 1 mM Mannitol; lane 6, DMSO (1 M); lane 7, 1 mM NaN_3; lane 8, 10 mM NaN_3; lane 9, 20 mM NaN_3; lane 10, 30 mM NaN_3; lane 11, 50 mM NaN_3; lane 12, 100 mM NaN_3.	298
Figure 6.25	Effect of various scavengers on the cleavage of pBR322 by 120 μM complex **VODMPhen**. Lane 1, Gene Ruler 1 kb DNA ladder; Lane 2, DNA alone; Lane 3, DNA +120 μM complex **VODMPhen** + H_2O_2. Lanes 4 – 12 involves reaction of 120 μM complex **VODMPhen** + H_2O_2 with DNA in presence of various scavengers; lane 4, t-butyl alcohol (1 M); lane 5, 1 mM Mannitol; lane 6, DMSO (1 M); lane 7, 1 mM NaN_3; lane 8, 10 mM NaN_3; lane 9, 20 mM NaN_3; lane 10, 30 mM NaN_3; lane 11, 50 mM NaN_3; lane 12, 100 mM NaN_3.	298
Figure 6.26	Effect of various scavengers on the cleavage of pBR322 by 25 μM complex **VODPPhen**. Lane 1, Gene Ruler 1 kb DNA ladder; Lane 2, DNA alone; Lane 3, DNA + 25 μM complex **VODPPhen** + H_2O_2. Lanes 4 – 12 involves reaction of 25 μM complex **VODPPhen** + H_2O_2 with DNA in presence of various scavengers; lane 4, t-butyl alcohol (1 M); lane 5, 1 mM Mannitol; lane 6, DMSO (1 M); lane 7, 1 mM NaN_3; lane 8, 10 mM NaN_3; lane 9, 20 mM NaN_3; lane 10, 30 mM NaN_3; lane 11, 50 mM NaN_3; lane 12, 100 mM NaN_3.	299
Figure 6.27	Effect of various scavengers on the cleavage of pBR322 by 120 μM complex **VODMPPhen**. Lane 1, Gene Ruler 1 kb DNA ladder; Lane 2, DNA alone; Lane 3, DNA +120 μM complex **VODMPPhen** + H_2O_2. Lanes 4 – 12 involves reaction of 120 μM complex **VODMPPhen** + H_2O_2 with DNA in presence of various scavengers; lane 4, t-butyl alcohol (1 M); lane 5, 1 mM Mannitol; lane 6, DMSO (1 M); lane 7, 1 mM NaN_3; lane 8, 10 mM NaN_3; lane 9, 20 mM NaN_3; lane 10, 30 mM NaN_3; lane 11, 50 mM NaN_3; lane 12, 100 mM NaN_3.	299

LIST OF FIGURES

Page

Appendix A UV-Vis spectrum of complex $NaVO_3$ (6.24×10^{-5} mol L^{-1}; A = 264 nm, ε = 2402 $mol^{-1}Lcm^{-1}$; A = 205 nm, ε = 7491 $mol^{-1}Lcm^{-1}$) 323

Appendix B UV-Vis spectrum of complex $VOSO_4$ (4.73×10^{-5} mol L^{-1}; A = 206 nm, ε = 3087 $mol^{-1}Lcm^{-1}$; A = 201 nm, ε = 2949 $mol^{-1}Lcm^{-1}$) 323

Appendix C UV-Vis spectrum of complex $CuSO_4$ (1.35×10^{-4} mol L^{-1}; A = 237 nm, ε = 3431 $mol^{-1}Lcm^{-1}$) 324

Appendix D UV-Vis spectrum of complex $CuCl_2$ (8.92×10^{-5} mol L^{-1}; A = 235 nm, ε = 3360 $mol^{-1}Lcm^{-1}$) 324

LIST OF TABLES

		Page
Table 1.1	Some of metal ions in clinical use	3
Table 1.2	The antibacterial and antiproliferative activities of some vanadium, copper and manganese complexes	5
Table 2.1	List of chemicals used in the synthesis	30
Table 2.2	List of complexes have been synthesized	37
Table 3.1	Crystal data, data collection and structure refinement parameters of complex **VO_2PP**	50
Table 3.2	Selected bond lengths (Å) and bond angles (°) of complex **VO_2PP**	52
Table 3.3	Hydrogen bonding distances and angles of complex **VO_2PP**	52
Table 3.4	Crystal data, data collection and structure refinement parameters of complex **VO_2GLY**	54
Table 3.5	Selected bond lengths (Å) and bond angles (°) of complex **VO_2GLY**	57
Table 3.6	Hydrogen bonding distances and angles of complex **VO_2GLY**	57
Table 3.7	Crystal data, data collection and structure refinement parameters of complex **VOPYDC**	59
Table 3.8	Selected bond lengths (Å) and bond angles (°) of complex **VOPYDC**	62
Table 3.9	Hydrogen bonding distances and angles of complex **VOPYDC**	62
Table 3.10	FT-IR analysis data of complexes **VO_2PP**, **VO_2GLY** and **VO_2HPYDC**	65
Table 3.11	FT-IR analysis data of complexes **VOPYDC** and **VOMAL**	71
Table 3.12	The UV-Vis analysis data of complexes **VO_2PP**, **VO_2GLY**, **VO_2HPYDC**, **VOPYDC** and **VOMAL**	76

LIST OF TABLES

Page

Table 3.13 The ^{51}V-NMR chemical shift of complexes **VO_2PP**, **VO_2GLY**, **VO_2HPYDC**, **VOPYDC** and **VOMAL** 84

Table 3.14 The Epa, Epc, ΔEp and $E_{1/2}$ values of complexes **VO_2PP**, **VO_2GLY**, **VOPYDC**, **VOMAL** and **VO_2HPYDC** 90

Table 3.15 Concentration of complexes **VO_2PP**, **VO_2GLY**, **VOPYDC**, **VOMAL** and **VO_2HPYDC** that induce total cleavage of supercoil DNA 101

Table 3.16 Antibacterial activity of complexes **VO_2PP**, **VO_2GLY**, **VOPYDC**, **VOMAL, VO_2HPYDC**, $VOSO_4$ and $NaVO_3$, results correspond to diameter of the inhibition zone(mm) 109

Table 3.17 Antibacterial activity of complexes **VOPYDC**, **VO_2HPYDC** and $VOSO_4$, the results are expressed as MIC (minimal inhibitory concentration) 110

Table 3.18 Antiproliferative activity of complexes **VO_2PP**, **VO_2GLY**, **VOPYDC**, **VOMAL** and **VO_2HPYDC** towards human cancer cell lines 112

Table 4.1 Crystal data, data collection and structure refinement parameters of complexes **Cu-4-Cl-2-NO_2BZO** and **Cu-2-Cl-4-NO_2BZO** 115

Table 4.2 Crystal data, data collection and structure refinement parameters of complexes **Cu-2-Cl-6-FBZO** and **Cu-2-F-6-FBZO** 116

Table 4.3 Crystal data, data collection and structure refinement parameters of complexes **Cu-2-ClBZO** and **Cu-2-BrBZO** 117

Table 4.4 Selected bond lengths (Å) and bond angles (°) of complex **Cu-4-Cl-2-NO_2BZO** 120

Table 4.5 Hydrogen bonding distances and angles of complex **Cu-4-Cl-2-NO_2BZO** 120

Table 4.6 Selected bond lengths (Å) and bond angles (°) of complex **Cu-2-Cl-4-NO_2BZO** 123

LIST OF TABLES

Page

Table 4.7 Hydrogen bonding distances and angles of complex **Cu-2-Cl-4-NO$_2$BZO** 124

Table 4.8 Selected bond lengths (Å) and bond angles (°) of **Cu-2-Cl-6-FBZO** 126

Table 4.9 Hydrogen bonding distances and angles of **Cu-2-Cl-6-FBZO** 126

Table 4.10 Selected bond lengths (Å) and bond angles (°) of **Cu-2-F-6-FBZO** 129

Table 4.11 Hydrogen bonding distances and angles of **Cu-2-F-6-FBZO** 129

Table 4.12 Selected bond lengths (Å) and bond angles (°) of complex **Cu-2-ClBZO** 132

Table 4.13 Hydrogen bonding distances and angles of **Cu-2-ClBZO** 132

Table 4.14 Selected bond lengths (Å) and bond angles (°) of complex **Cu-2-BrBZO** 135

Table 4.15 Hydrogen bonding distances and angles of **Cu-2-BrBZO** 135

Table 4.16 Crystal data, data collection and structure refinement parameters of complex **CuP-5-Cl-2-NO$_2$BZO** 137

Table 4.17 Selected bond lengths (Å) and bond angles (°) of complex **CuP-5-Cl-2-NO$_2$BZO** 141

Table 4.18 Hydrogen bonding distances and angles of complex **CuP-5-Cl-2-NO$_2$BZO** 141

Table 4.19 FT-IR analysis data of complexes **Cu-4-Cl-2-NO$_2$BZO**, **Cu-2-Cl-4-NO$_2$BZO**, **CuP-5-Cl-2-NO$_2$BZO**, **Cu-2-Cl-6-FBZO**, **Cu-2-F-6-FBZO**, **Cu-2-ClBZO** and **Cu-2-BrBZO** 144

Table 4.20 The UV-Vis analysis data of complexes **Cu-4-Cl-2-NO$_2$BZO**, **Cu-2-Cl-4-NO$_2$BZO**, **CuP-5-Cl-2-NO$_2$BZO**, **Cu-2-Cl-6-FBZO**, **Cu-2-F-6-FBZO**, **Cu-2-ClBZO** and **Cu-2-BrBZO** 154

LIST OF TABLES

		Page
Table 4.21	The Epa, Epc, ΔEp and $E_{1/2}$ values of complexes **Cu-4-Cl-2-NO_2BZO**, **Cu-2-Cl-4-NO_2BZO**, **CuP-5-Cl-2-NO_2BZO**, **Cu-2-Cl-6-FBZO**, **Cu-2-F-6-FBZO**, **Cu-2-ClBZO** and **Cu-2-BrBZO**	164
Table 4.22	Concentration of complexes **Cu-4-Cl-2-NO_2BZO**, **Cu-2-Cl-4-NO_2BZO**, **CuP-5-Cl-2-NO_2BZO**, **Cu-2-Cl-6-FBZO**, **Cu-2-F-6-FBZO**, **Cu-2-ClBZO** and **Cu-2-BrBZO** that induce total cleavage of supercoil DNA	177
Table 4.23	Antibacterial activity of complexes **Cu-4-Cl-2-NO_2BZO**, **Cu-2-Cl-4-NO_2BZO**, **CuP-5-Cl-2-NO_2BZO** and **Cu-2-Cl-6-FBZO**, results correspond to diameter of the inhibition zone (mm)	186
Table 4.24	Antibacterial activity of complexes **Cu-2-F-6-FBZO**, **Cu-2-ClBZO** and **Cu-2-BrBZO**, $CuCl_2$ and $CuSO_4$, results correspond to diameter of the inhibition zone (mm)	187
Table 4.25	Antibacterial activity of complexes **Cu-4-Cl-2-NO_2BZO**, **Cu-2-Cl-4-NO_2BZO**, **CuP-5-Cl-2-NO_2BZO**, **Cu-2-Cl-6-FBZO**, **Cu-2-F-6-FBZO**, **Cu-2-ClBZO** and **Cu-2-BrBZO** against Gram negative bacteria Enterobacter aerogenes, the results are expressed as MIC (minimal inhibitory concentration)	188
Table 4.26	Antiproliferative activity of complexes **Cu-4-Cl-2-NO_2BZO**, **Cu-2-Cl-4-NO_2BZO**, **CuP-5-Cl-2-NO_2BZO** and **Cu-2-Cl-6-FBZO** towards human cancer cell lines	190
Table 4.27	Antiproliferative activity of complexes **Cu-2-F-6-FBZO** and **Cu-2-ClBZO** towards human cancer cell lines	191
Table 5.1	Crystal data, data collection and structure refinement parameters of complexes **MnP-4-Cl-2-NO_2BZO** and **MnP-3-NO_2-5-NO_2BZO**	194
Table 5.2	Crystal data, data collection and structure refinement parameters of complex **Mn-4-NO_2BZO**	195
Table 5.3	Selected bond lengths (Å) and bond angles (°) of complex **MnP-4-Cl-2-NO_2BZO**	197

LIST OF TABLES

Page

Table 5.4 Hydrogen bonding distances and angles of complex **MnP-4-Cl-2-NO_2BZO** 197

Table 5.5 Selected bond lengths (Å) and bond angles (°) of complex **MnP-3-NO_2-5-NO_2BZO** 199

Table 5.6 Hydrogen bonding distances and angles of complex **MnP-3-NO_2-5-NO_2BZO** 200

Table 5.7 Selected bond lengths (Å) and bond angles (°) of complex **Mn-4-NO_2BZO** 202

Table 5.8 Hydrogen bonding distances and angles of complex **Mn-4-NO_2BZO** 202

Table 5.9 Crystal data, data collection and structure refinement parameters of complex **MnP-4-NH_2BZO** 204

Table 5.10 Selected bond lengths (Å) and bond angles (°) of complex **MnP-4-NH_2BZO** 207

Table 5.11 Hydrogen bonding distances and angles of complex **MnP-4-NH_2BZO** 207

Table 5.12 Crystal data, data collection and structure refinement parameters of complex **MnP-4-FBZO** 209

Table 5.13 Selected bond lengths (Å) and bond angles (°) of complex **MnP-4-FBZO** 212

Table 5.14 Hydrogen bonding distances and angles of complex **MnP-4-FBZO** 212

Table 5.15 Crystal data, data collection and structure refinement parameters of complex **MnPGLY** 214

Table 5.16 Selected bond lengths (Å) and bond angles (°) of complex **MnPGLY** 217

Table 5.17 Hydrogen bonding distances and angles of complex **MnPGLY** 217

LIST OF TABLES

Page

Table 5.18 The FT-IR analysis data of complexes **MnP-4-Cl-2-NO_2BZO**, **MnP-3-NO_2-5-NO_2BZO**, **Mn-4-NO_2BZO**, **MnP-4-NH_2BZO**, **MnP-4-FBZO**, **MnP-4-ClBZO**, **MnPGLY** and **MnPyr** 222

Table 5.19 The UV-Vis analysis data of complexes **MnP-4-Cl-2-NO_2BZO**, **MnP-3-NO_2-5-NO_2BZO**, **Mn-4-NO_2BZO**, **MnP-4-NH_2BZO**, **MnP-4-FBZO**, **MnP-4-ClBZO**, **MnPGLY** and **MnPyr** 233

Table 5.20 The Epa, Epc, ΔEp and $E_{1/2}$ values of complexes **MnP-4-Cl-2-NO_2BZO**, **MnP-3-NO_2-5-NO_2BZO**, **Mn-4-NO_2BZO**, **MnP-4-NH_2BZO**, **MnP-4-FBZO**, **MnP-4-ClBZO**, **MnPGLY** and **MnPyr** 244

Table 5.21 Concentration of complexes **MnP-4-Cl-2-NO_2BZO**, **MnP-3-NO_2-5-NO_2BZO**, **Mn-4-NO_2BZO**, **MnP-4-NH_2BZO**, **MnP-4-FBZO**, **MnP-4-ClBZO**, **MnPGLY** and **MnPyr** that induce total cleavage of supercoil DNA 259

Table 5.22 Antibacterial activity of complexes **MnP-4-Cl-2-NO_2BZO**, **MnP-3-NO_2-5-NO_2BZO**, **Mn-4-NO_2BZO**, **MnP-4-NH_2BZO**, results correspond to diameter of the inhibition zone (mm) 266

Table 5.23 Antibacterial activity of complexes **MnP-4-FBZO**, **MnP-4-ClBZO**, **MnPGLY**, **MnPyr** and $MnCl_2$, results correspond to diameter of the inhibition zone (mm) 267

Table 5.24 Antiproliferative activity of complexes **MnP-4-Cl-2-NO_2BZO**, **MnP-3-NO_2-5-NO_2BZO**, **Mn-4-NO_2BZO**, **MnP-4-NH_2BZO** and **MnPyr** towards human cancer cell lines 269

Table 6.1 FT-IR analysis data of complexes **VOPhen**, **VODMPhen**, **VODPPhen** and **VODMPPhen** 273

Table 6.2 The UV absorption data of complexes **VOPhen**, **VODMPhen**, **VODPPhen** and **VODMPPhen** upon addition of increasing concentration of CT-DNA 285

Table 6.3 Antibacterial activity of complexes **VOPhen**, **VODMPhen**, **VODPPhen** and **VODMPPhen**, results correspond to diameter of the inhibition zone (mm) 302

LIST OF TABLES

Page

Table 6.4 Antibacterial activity of complexes **VOPhen**, **VODMPhen**, **VODPPhen** and **VODMPPhen**, the results are expressed as MIC (minimal inhibitory concentration) 303

LIST OF ABBREVIATIONS AND SYMBOLS

Cu-2-F-6-FBZO	tetrakis(μ-2,6-diflourobenzoato-κ̣^{2}*O*,*O*’)bis[aquacopper(II)]
Cu-2-BrBZO	tetrakis(μ-2-bromobenzoato-κ̣^{2}*O*,*O*’)bis[aquacopper(II)]
Cu-2-Cl-4-NO$_2$BZO	tetrakis(μ-2-chloro-4-nitrobenzoato-κ̣^{2}*O*,*O*’) bis[aquacopper(II)]
Cu-2-Cl-6-FBZO	tetrakis(μ-2-chloro-6-fluorobenzoato-κ^2*O*,*O*’) bis[aquacopper(II)]
Cu-2-ClBZO	tetrakis(μ-2-chloro-benzoato-κ^2*O*,*O*’)bis[aquacopper(II)]
Cu-4-Cl-2-NO$_2$BZO	tetrakis(μ-4-chloro-2-nitrobenzoato-κ̣^{2}*O*,*O*’) bis[aquacopper(II)]
CuP-5-Cl-2-NO$_2$BZO	catena-poly[[bis(5-chloro-2-nitrobenzoato)copper(II)] bis(μ-5-chloro-2- nitrobenzoato)]
Hela	Human cervical cancer cell line
HepG2	Human liver cancer cell line
IC$_{50}$	A measure of the concentration of particular drug that inhibit the biological process of cells by half
bp	base pair
LC$_{50}$	A measure of the concentration of particular drug that kill 50 % of the cells
LMCT	Ligand to Metal Charge Transfer
MCF-7	Human breast cancer cell line
MDA-MB-231	Human invasive breast cancer cell line
MIC	minimal inhibitory concentration
Mn-4-NO$_2$BZO	tetraaquabis(4-nitrobenzoato)manganese(II) hydrate

LIST OF ABBREVIATIONS AND SYMBOLS

MnP-4-ClBZO	catena-poly[[diaquabis(4-chlorobenzoato) manganese(II)]bis(μ-4-chlorobenzoato)]
MnP-4-Cl-2-NO_2BZO	catena-poly[[diaquabis(4-chloro-2-nitrobenzoato) manganese(II)]bis(μ-4-chloro-2-nitrobenzoato)]
MnP-4-FBZO	catena-poly[[diaquabis(4-flourobenzoato) manganese(II)]bis(μ-4-flourobenzoato)]
MnP-4-NH_2BZO	catena-poly[[bis(4-aminobenzoato)manganese(II)] tri(μ-4-aminobenzoato)]
MnPGLY	catena-poly[[aqua(diglycolato)manganese(II) hydrate)] bis(μ-diglycolato)]
MnPyr	diaquabis(pyridine-2-carboxylato)manganese(II) hydrate
MTT	(3-[4,5-dimethylthiazol-2-yl]-2,5-diphenyltetrazolium bromide)
NMR	Nuclear Magnetic Resonance
ROS	Reactive oxygen species
SRB	Sulforhodamine B
TGI	Cytostatic activity = A measure of the concentration of particular drug that inhibit total growth of cell lines.
UV-Vis	Ultraviolet-Visible
VO_2GLY	sodium (diglycolato)dioxovanadium(V) dihydrate
VO_2HPYDC	Sodium (4-hydroxypyridine-2,6-dicarboxylato) dioxovanadium(V) dihydrate
VO_2PP	(pyridine-2-carboxylato)(pyridinium-2-carboxylato) dioxovanadium(V) monohydrate

LIST OF ABBREVIATIONS AND SYMBOLS

VODMPhen	aqua(2,9-dimethyl-1,10-phenanthroline) sulfatooxovanadium(IV)
VODMPPhen	aqua(2,9-dimethyl-4,7-diphenyl-1,10-phenanthroline) sulfatooxovanadium(IV) hydrate
VODPPhen	aqua(4,7-diphenyl-1,10-phenanthroline) sulfatooxovanadium(IV) hydrate
VOMAL	disodium diaquabis(malonato)oxovanadium(IV)
VOPhen	aqua(1,10-phenanthroline)sulfatooxovanadium(IV)
VOPYDC	diaqua(pyridine-2,6-carboxylato)oxovanadium(IV)ethanol solvate
ΔEp	| Epa – Epc |
$\mathbf{V^{V}}$	Vanadium V
$\mathbf{V^{IV}}$	Vanadium IV
ε	Molar absorptivity

SINTESIS, PENCIRIAN, SIFAT-SIFAT NUCLEOLITIK, ANTIBAKTERIA DAN ANTIPOLIFERATIF BAGI KOMPLEKS VANADIUM, KUPRUM DAN MANGAN

Abstrak

Siri kompleks bagi vanadium karboksilato, kuprum karboksilato, mangan karboksilato dan terbitan vanadium fenantrolina telah disintesis dan dicirikan. Maklumat penuh tentang kompleks ditunjukkan dalam Jadual 2.2 (muka surat 37). Kompleks ini telah dicirikan dengan menggunakan kristalografi X-ray, analisis unsur, FT-IR, spektroskopi UV–Vis dan siklik voltammetrik. Dalam kajian elektrokimia, kompleks vanadium karboksilato telah menunjukkan aktif redok dengan mempamerkan pasangan redok kuasi-berbalik yang selaras dengan V^V/V^{IV} proses redok, manakala kompleks kuprum karboksilato telah menunjukkan aktif redok dengan mempamerkan dua pasangan redok kuasi-berbalik yang selaras dengan $Cu^{II}Cu^{II}/Cu^{II}Cu^{I}$ dan $Cu^{II}Cu^{I}/Cu^{I}Cu^{I}$ proses redok dan mangan karboksilato telah menunjukkan aktif redok dengan mempamerkan pasangan redok kuasi-berbalik yang selaras dengan Mn^{II}/Mn^{III} proses redok. Dalam kajian nukleolitik, semua kompleks didapati boleh mengakibatkan pengoksidaan belahan DNA tetapi dengan cara yang berbeza. Kompleks kuprum karboksilato dan mangan karboksilato boleh mengakibatkan belahan DNA dalam kehadiran H_2O_2. Sementara itu, untuk kompleks vanadium karboksilato, kompleks vanadium(V) karboksilato memerlukan H_2O_2 untuk mengakibatkan belahan DNA manakala kompleks

vanadium(IV) karboksilato tidak memerlukan H_2O_2 untuk mengakibatkan belahan DNA. Bagi kompleks terbitan vanadium fenantrolina pula, mereka boleh mengakibatkan belahan DNA dalam kehadiran H_2O_2 dan dalam keadaan tanpa H_2O_2. Walaubagaimanapun, aktiviti belahan DNA meningkat secara mendadak dalam kehadiran H_2O_2. Agen perencet reaktif spesis oksigen (ROS) juga telah digunakan untuk menentukan spesis reaktif yang bertanggunjawab dalam belahan DNA. Hidroksil radikal dan oksigen tunggal adalah ROS yang bertanggunjawab dalam belahan DNA. Dalam penyaringan antibakteria, semua kompleks kecuali kompleks mangan karboksilato mempamerkan aktiviti antibakteria terhadap spesis bakteria Gram positif atau Gram negatif. Kompleks kuprum karboksilato menunjukkan aktiviti antibakteria yang sangat selektif di mana mereka hanya menunjukkan aktiviti antibakteria terhadap *Enterobacter aerogenes* berGram negatif bakteria. Aktiviti antibakteria kompleks terbitan vanadium fenantrolina telah menunjukan bahawa kumpulan metil yang terikat pada kedudukan 2 dan 9 pada gelang fenantrolina dapat meningkatkan aktiviti antibakteria. Dalam penyaringan antipoliferatif, secara umum kompleks vanadium karboksilato mempamerkan aktiviti antipoliferatif yang lebih tinggi berbanding dengan kompleks kuprum karboksilato dan mangan karboksilato. Kompleks kuprum karboksilato dan mangan karboksilato menunjukkan selektiviti sitotoksik terhadap garisan sel kanser HepG2 apabila dibandingkan dengan garisan sel kanser MCF-7 dan Hela. Eksperimen nukleolitik telah menyarankan bahawa belahan atau fragmentasi DNA oleh ROS yang dihasilkan oleh kompleks berkemungkinan besar bertangungjawab terhadap aktiviti antipoliferatif yang dipamerkan oleh kompleks.

Synthesis, Characterization, Nucleolytic, Antibacterial and Antiproliferative Properties of Vanadium, Copper and Manganese Complexes

ABSTRACT

Series of vanadium carboxylato complexes, copper carboxylato complexes, manganese carboxylato complexes and vanadium phenanthroline derivative complexes have been synthesized and characterized. The details of all the complexes are tabulated in Table 2.2 (page 37). The complexes have been characterized by X-ray crystallography, elemental analysis, FT-IR, UV–Vis spectroscopy and cyclic voltammetry. In electrochemistry studies, vanadium carboxylato complexes show redox active by displaying a quasi-reversible redox couple corresponding to V^{V}/V^{IV} redox process while copper carboxylato complexes show redox active by displaying two quasi-reversible redox couples corresponding to $Cu^{II}Cu^{II}/Cu^{II}Cu^{I}$ and $Cu^{II}Cu^{I}/Cu^{I}Cu^{I}$ redox processes and manganese carboxylato complexes show redox active by displaying a quasi-reversible redox couple corresponding to Mn^{II}/Mn^{III} redox process. In nucleolytic studies, all the complexes can induce oxidative DNA cleavage but in different manner. The copper carboxylato complexes and manganese carboxylato complexes can induce DNA cleavage in the presence of H_2O_2. Meanwhile for vanadium carboxylato complexes, vanadium(V) carboxylato complexes require H_2O_2 to induce DNA cleavage while vanadium(IV) carboxylato complexes do not require H_2O_2 to induce DNA cleavage. As for vanadium phenanthroline derivative complexes, they can induce DNA cleavage in the presence and in the absence of H_2O_2. However, the DNA cleavage activity of the vanadium phenanthroline derivative complexes is greatly enhanced in the presence of H_2O_2. Reactive oxygen species (ROS) scavengers have also been used to ascertain the reactive species responsible for DNA cleavage. The hydroxyl radical and singlet oxygen species have been found to be the ROS that are responsible in the DNA cleavage reaction. In the antibacterial screening, all the complexes except manganese carboxylato complexes exhibit antibacterial activity against certain Gram negative or Gram positive bacteria species. Copper carboxylato complexes show a very selective antibacterial activity whereby they only exhibit antibacterial activity against Gram negative bacteria Enterobacter aerogenes. The antibacterial activity of vanadium phenanthroline derivative complexes reveals that methyl groups attached at the position 2 and 9 in phenanthroline ring may increase the complexes antibacterial activity. In antiproliferative screening, vanadium carboxylato complexes in general exhibit higher antiproliferative activity when compared to copper carboxylato complexes and manganese carboxylato complexes. Copper carboxylato complexes and manganese carboxylato complexes exhibit cytotoxic selectivity against HepG2 cancer cell line when compared to MCF-7 and Hela cancer cell lines. The nucleolytic experiments suggest that the cleavage or fragmentation of DNA by ROS generated by the complexes maybe responsible for the antiproliferative activity exhibited by the complexes.

Keywords: Vanadium Complexes; Copper Complexes; Manganese Complexes; DNA Cleavage; Antibacterial; Antiproliferative

CHAPTER 1

INTRODUCTION

1.1 Biological roles and medicinal applications of metal complexes and metal ions

Studies on biological activities of metal complexes have been one of our long-term interests. Metal complexes are well known to exhibit antibacterial, antiproliferative, antiapoptotic, anti-inflammatory and insulin mimetic properties [1-28]. Several of the metal complexes have entered clinical trials and few have been registered for clinical use [29-31]. Platinum based complexes such as cisplatin, carboplatin and oxaliplatin are widely used as chemotherapeutic agents against ovarian, lung, head, neck and colorectal cancers, and have greatly improving the survival rates of patients worldwide. Schematic structures of cisplatin, carboplatin and oxaliplatin are depicted in Figure 1.1. These platinum complexes react *in vivo*, crosslink the DNA in several different ways and subsequently interfering the cell division by mitosis. The damaged DNA elicits DNA repair mechanisms, which in turn activate apoptosis when repair proves impossible. Meanwhile, Aurum(I) thiolate drugs such as aurothiomalate (Myocrisin^R), aurothioglucose (Solganol^R), aurothiopropanol sulfonate (Allochrysin^R), and the oral drug auranofin (Ridaura^R), are widely used for the treatment of difficult cases of rheumatoid arthritis. Bismuth(III) compounds such as bismuth subcitrate and subsalicylate are widely used for the treatment of diarrhoea, dyspepsia and gastric and duodenal ulcers. Bismuth(III) compounds are found to be antibacterial active against bacteria Helicobacter pylori which is associated with the mucus layer of ulcers. Sodium nitroprusside ($Na_2[Fe^{II}(CN)_5(NO)]\cdot 2H_2O$ or (Nipride^R) is used to treat hypotensive while Cu-salicylate (Alcusal^R) is used to treat inflammatory. The success of metal complexes in medicinal applications has aroused great interest in the development of new metal complexes to diagnose and treat diseases including cancers, bacteria and virus infection related diseases, inflammatory and diabetes.

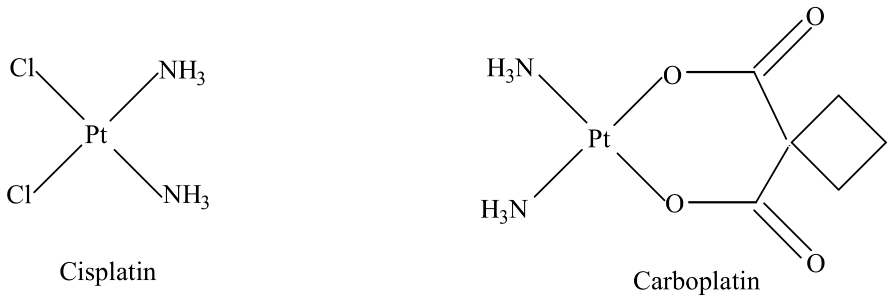

Cisplatin

Carboplatin

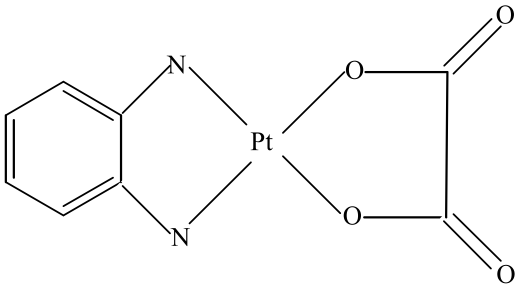

oxaliplatin

Figure 1.1: Schematic structures of cisplatin, carboplatin and oxaliplatin

Apart from metal complexes, metal ion or inorganic elements play essential roles in biological and biomedical processes in human health and disease as metalloenzymes and metalloproteins [29]. As metalloproteins, metal ions perform as catalyst or stabilizer to stabilize the protein tertiary or quaternary structure. In addition, many proteins need to bind one or more metal ions to perform their functions. Complex zinc ion is one of the most important components of metalloproteins in the human body, which functions as DNA transcription and regulation as well as oxidation and hydrolysis, cleavage of peptide bonds as well as formation of phosphodiester bonds. Meanwhile, copper ion is presence in some of the most important metalloenzymes in the human body and functions as superoxide dismutase to neutralize free radical generated from various human biological systems. Metal ions are also very important for the structure and function (in the case of RNA) of nucleic acids. Besides, many organic compounds used in medicine do not have a purely organic mode of action; some are activated or biotransformed by metal ions including metalloenzymes, others have a direct or indirect effect on metal ion metabolism. Some of the metal ions have also been registered for clinical used as therapy and diagnosis agents, as listed in Table 1.1.

Table 1.1: Some of metal ions in clinical use

Compounds	Function/Treat
Li_2CO_3	Prophylaxis for bipolar disorders
$CaCO_3$, $Mg(OH)_2$	Antacid
$La_2^{III}(CO_3)_3$	Chronic renal failure
$MgSO_4$	Hypomagnesemia
Potassium citrate	Kidney stones
Magnesium citrate	Saline laxative

1.2 Antibacterial and antiproliferative activities of transition metal complexes

Transition metal complexes such as vanadium, copper and manganese complexes are known to exhibit excellent antibacterial and antiproliferative activities. The summary of antibacterial and antiproliferative activities of selected few vanadium, copper and manganese complexes that have already described in the literatures is tabulated in Table 1.2. Referring to Table 1.2, it can be seen that transition metal complexes are rich in antibacterial and antiproliferative activities, being active against a wide spectrum of bacteria species or cancer cells. Transition metal complexes may induce cell death through disruption of the cell cycle or by DNA strand scission [32]. There are evidences to indicate that metal complexes can induce DNA strand scission not directly reacting with DNA components but acting mainly through the production of highly reactive oxygen species, especially hydroxyl radicals generated in cells. These reactive oxygen species actually cause the DNA strand scission. Transition metal complexes through Fenton-like reactions and/or during the intracellular reduction can generate reactive oxygen species. Besides, some transition metal complexes, which are photoactivatable, can induce DNA cleavage upon UV irradiation and singlet oxygen is the common reactive oxygen species that is generated in this process. Rich diversity of antibacterial and antiproliferative activities by transition metal complexes provides exciting prospects for the design of novel therapeutic agents with unique mechanisms of action to act against certain bacteria or cancers, as different metal complexes can produce different therapeutic effect. Therefore, detailed investigations could be helpful in designing more potent antibacterial and anticancer agents for the therapeutic use.

Table 1.2: The antibacterial and antiproliferative activities of some vanadium, copper and manganese complexes

Complexes	Antibacterial/ Antiproliferative activity	Bacteria species/Cancer cells	Ref:
[Cu^{II}(4-(2-pyridylmethyl)-1,7-dimethyl-1,4,7-triazonane-2,6-dione)($CH_3CN)_2$]($ClO_4)_2$	Antibacterial	Escherichia coli (T7), Staphylococus aureus, Pseudomonas aeruginosa	13
Cu^{II}(2-furancarbaldehyde thiosemicarbazone) $0.5H_2O$	Antibacterial	Bacillus subtilis, Staphylococus aureus	18
[Cu_2^{II}(N,N'-bis(3-aminopropyl)oxamide)(2,2'-bipyridine)(2,4,6-trinitrophenol)(H_2O)](2,4,6-trinitrophenol)	Antibacterial	Escherichia coli, Bacillus subtilis, Staphylococus aureus	16
Cu^{II}_2(N,N'-bis(N-hydroxyethylaminoethyl) oxamide)(2,4,6-trinitrophenol)$_2$	Antiproliferative	SMMC-7721 human hepatocellular carcinoma cells, A549 human lung adenocarcinoma cells	8
Cu^{II} (ethyl 2-bis(2-pyridylmethyl)aminopropionate)Cl_2	Antiproliferative	Eca-109 human esophageal cancer cells, A549 human lung adenocarcinoma cells	10
Cu^{II} (norfloxacinato)(2,2'-bipyridine)Cl_2	Antiproliferative	HL-60 and K562 human leukemia cells	19

Table 1.2: Continued

Complexes	Antibacterial/ Antiproliferative activity	Bacteria species/Cancer cells	Ref:
Mn^{II}(tetraphenyl porphyrin), (ebselen–porphyrin conjugate)	Antibacterial	Staphylococus aureus	15
Mn^{II}(tetraamide macrocyclic)NO_3	Antibacterial	Pseudomonas cepacicola, Klebsella aerogenous	25
Mn^{II}(6,7-dicycanodipyrido[2,2-*d*:29,39-*f*]quinoxaline)(NO_3)(H_2O)]NO_3.CH_3OH	Antiproliferative	BGC-823 human stomach cancer cells, HL-60 human leukemia cells	27
$V^{V}{}_4O_{10}(\mu\text{-}O)_2$[VO(H-ciprofloxacin)$_2$)]$_2$.13$H_2O$	Antibacterial	Staphylococus aureus, Escherichia coli, Pseudomonas aeruginosa	21
V^{V} (2-methyl-3H-5-hydroxy-6-carboxy-4-pyrimidinone ethyl ester)	Antiproliferative	Hela human cervical cancer cells	6
$V^{V}O_2$(salicylaldehydesemicarbazone)	Antiproliferative	MC3T3-E1 osteoblastic mouse calvaria-derived cells, UMR106 rat osteosarcoma-derived cells	12
$V^{IV}O$(3-amino-6(7)-chloroquinoxaline-2-carbonitrile N^1, N^4-dioxide)$_2$	Antiproliferative	V79 chinese hamster lung fibroblasts cells	24

1.3 Background of nucleolytic activity of metal complexes

Recently, research on nucleolytic activity of metal complexes has blossomed leading to the discovery of the capacity of metal complexes to interact with DNA and further to induce DNA cleavage in the presence of co-factor. Transition metal complexes such as ruthenium, copper, cobalt, manganese and vanadium complexes have been reported to promote DNA cleavage in the presence of co-factor [33-55]. The DNA cleavage by metal complexes can occur via oxidative, photolytic and hydrolytic cleavage.

Double helical DNA consists of two complementary, antiparallel polydeoxyribonucleotide strands associated by specific hydrogen bonding interactions between nucleotide bases, Figure 1.2. The backbone of the DNA strand is made from alternating phosphate and sugar residues. The sugar in DNA is 2-deoxyribose, which is a pentose (five-carbon) sugar. The sugars are joined together by phosphate groups that form phosphodiester bonds between the third and fifth carbon atoms of adjacent sugar rings. The sugar phosphate backbone of paired strands defines the helical grooves, within which the edges of the heterocyclic bases are exposed. The biologically relevant B-form structure of the DNA double helix is characterized by a shallow, wide major groove and a deep, narrow minor groove. The major and minor grooves provide a lot of hydrogen binding sites. The DNA double helix is stabilized by hydrogen bonds between the nucleotide bases attached to the two strands. The four bases found in DNA are adenine, cytosine, guanine and thymine, Figure 1.3. These four bases are attached to the sugar/phosphate to form the complete nucleotide.

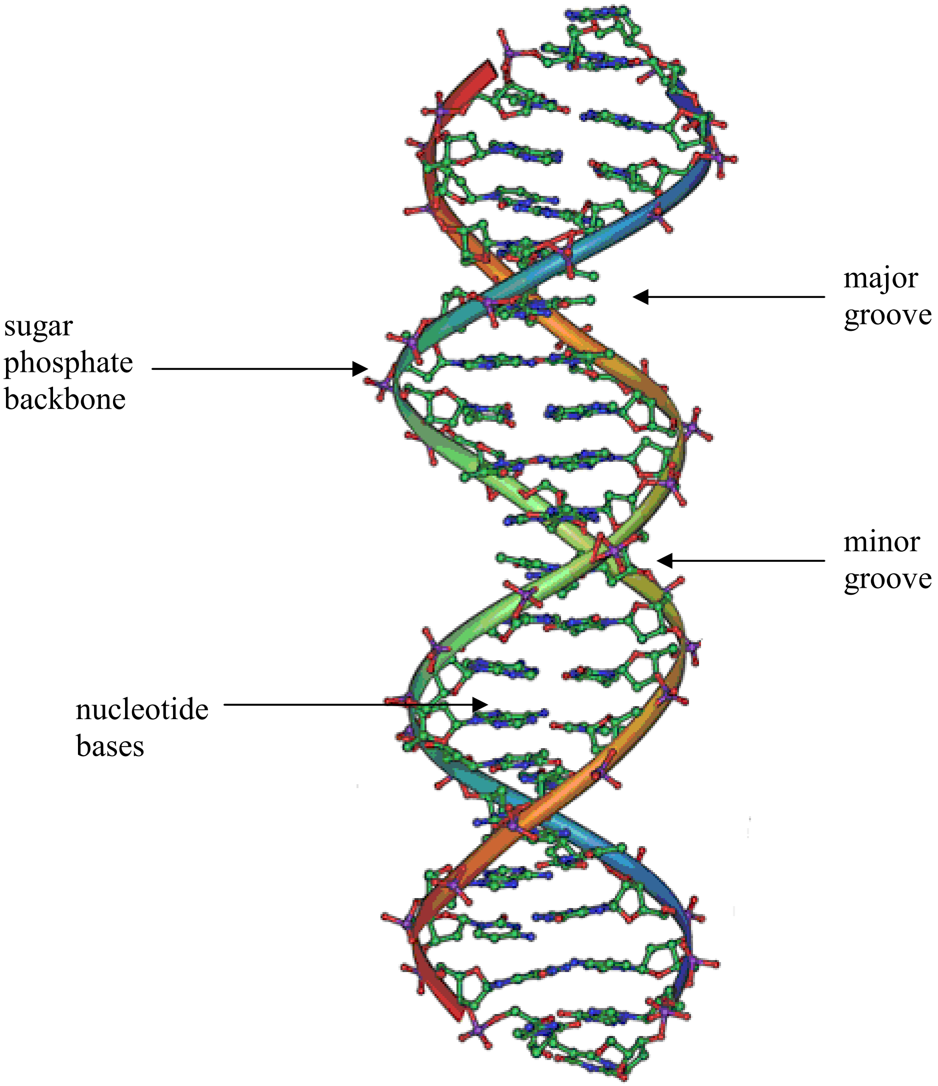

Figure 1.2: The structure of part of a DNA double helix

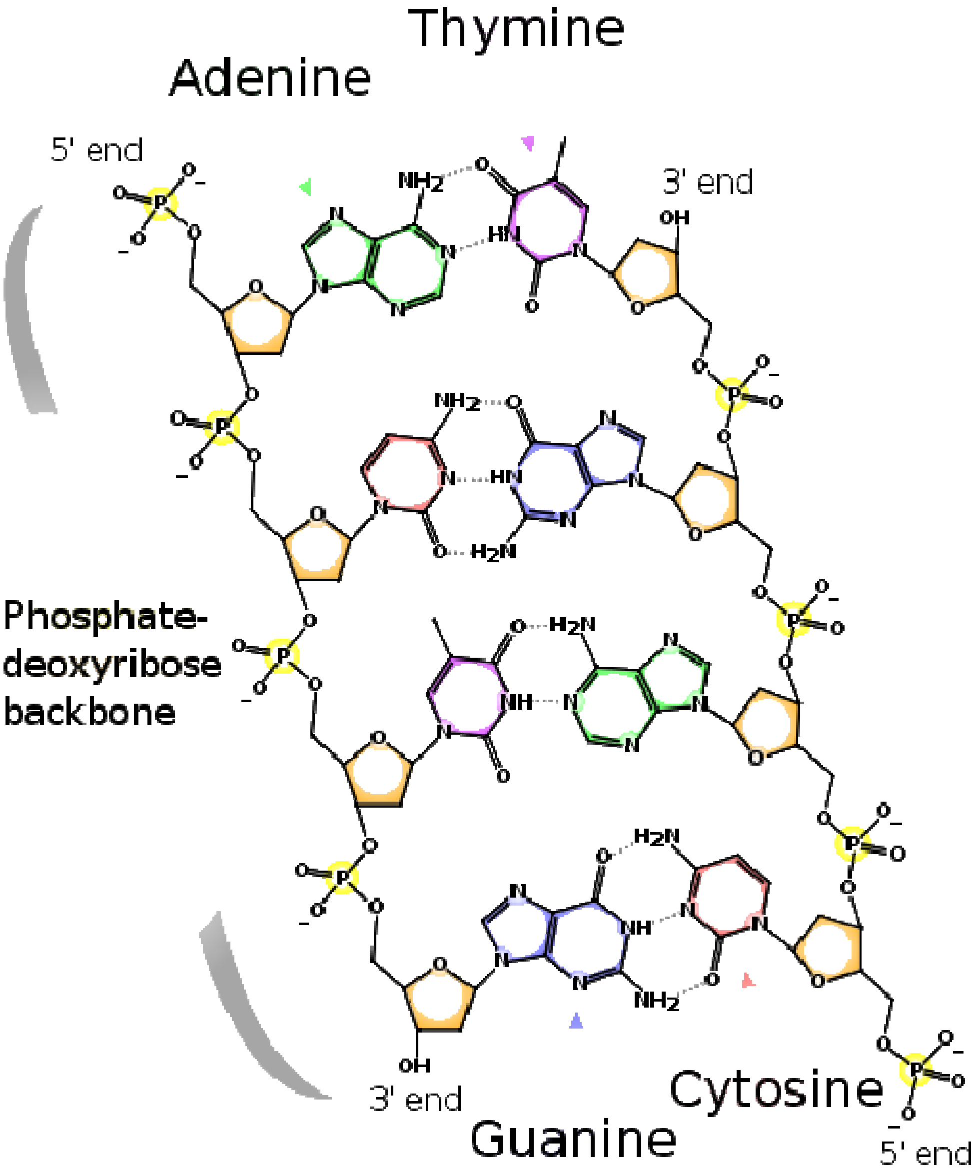

Figure 1.3: The chemical structure of DNA. Hydrogen bonds are shown as dotted lines

The DNA cleavage by metal complexes can be monitored by agarose gel electrophoresis. The DNA strain that was used in DNA cleavage studies is pBR322 DNA. The pBR322 DNA is a double helix DNA and it exists in supercoil form. In general, if scission or cleavage occurs on one strand of the supercoil DNA, the supercoil (Form I) will relax and convert to nicked form (Form II) while if scission occurs on both strands, a linear form (Form III) will be generated (Figure 1.4). These three forms of DNA will migrate in different rate in gel electrophoresis (Figure 1.5) with supercoil form migrates the fastest while nicked form migrates the slowest and linear form migrates in between supercoil and nicked forms. DNA cleavage by metal complexes is varied among the complexes, with some metal complexes can induce both single and double strand scissions while some metal complexes can only induce single scission.

In oxidative and photolytic DNA cleavage, metal complexes cannot induce DNA cleavage directly but indirectly through generating reactive oxygen species (ROS) such as hydroxyl radical and singlet oxygen. These ROS are actually responsible in DNA cleavage reaction. In order to study the DNA cleavage mechanism by metal complexes, various inhibiting agents have been used such as DMSO, t-butanol, mannitol and sodium azide. DMSO, t-butanol and mannitol are used as hydroxyl radical inhibitors while sodium azide is used as singlet oxygen inhibitor. Meanwhile in hydrolytic DNA cleavage, metal complexes can induce DNA cleavage directly by cleaving the P–O bonds in the phosphodiester of DNA.

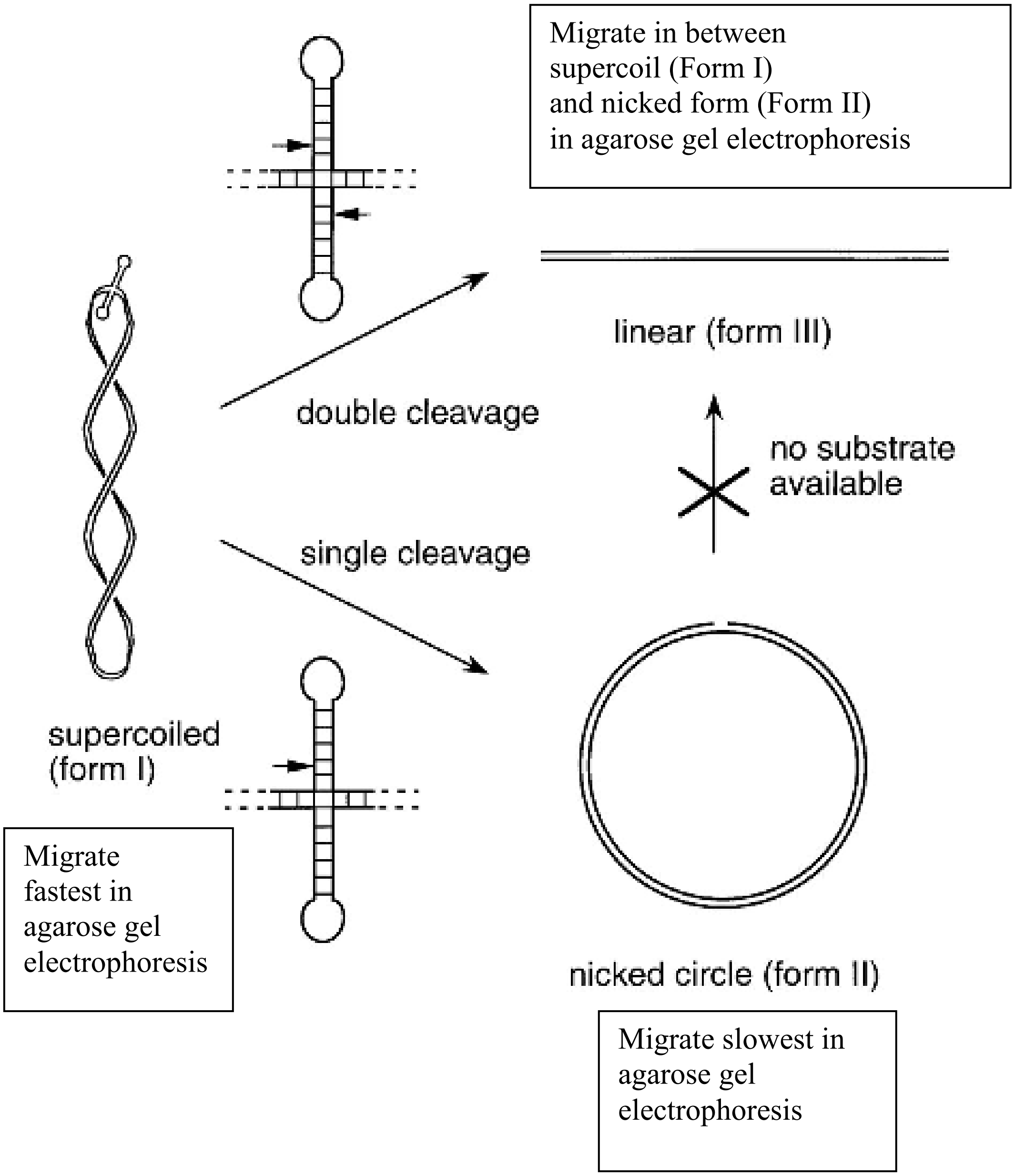

Migrate in between
supercoil (Form I)
and nicked form (Form II)
in agarose gel electrophoresis

Migrate
fastest in
agarose gel
electrophoresis

Migrate slowest in
agarose gel
electrophoresis

Figure 1.4: Supercoiled, nicked and linear DNA

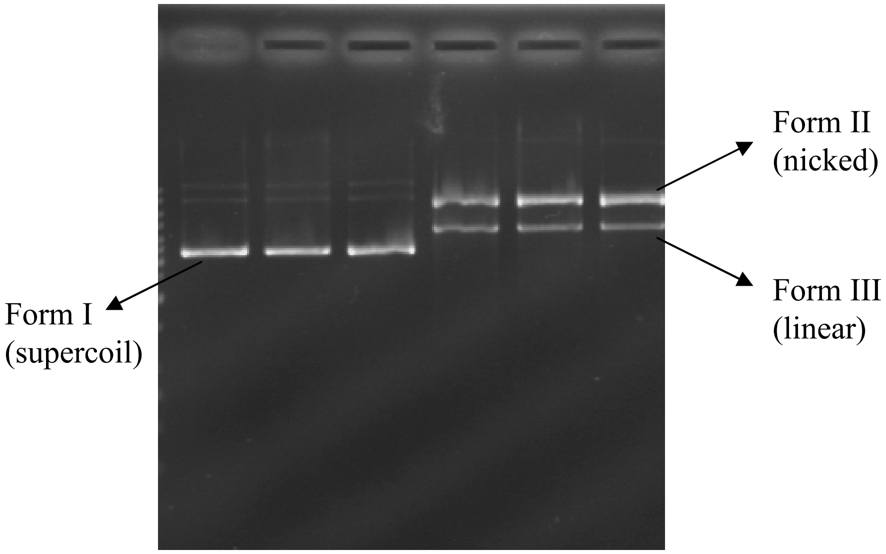

Figure 1.5: Supercoiled, nicked and linear DNA bands in gel electrophoresis diagram

1.3.1 Oxidative DNA cleavage by metal complexes in the presence of 3-mercaptopropionic acid (MPA)

Complexes $[Cu^{II}(ternary\text{-}L\text{-}glutamine)(1,10\text{-}phenanthroline)(H_2O)](ClO_4)$ and $[Cu^{II}(ternary\text{-}S\text{-}methyl\text{-}L\text{-}cysteine)(1,10\text{-}phenanthroline)(H_2O)](ClO_4)$ (Figure 1.6) can exhibit oxidative DNA cleavage in the presence of 3-mercaptopropionic acid (MPA) [33, 34]. MPA plays as reduction agent in the DNA cleavage reaction. Both of the complexes can only induce single DNA scission by converting supercoil DNA to nicked form. The mechanistic aspects of the DNA cleavage reactions have been investigated with various inhibiting agents and the results show that hydroxyl radical scavenger DMSO can inhibit the DNA cleavage induced by both of the complexes. This indicates the involvement of hydroxyl radical in the cleavage reaction. The proposed DNA cleavage mechanism of metal complex in the presence of MPA is illustrated in Figure 1.7.

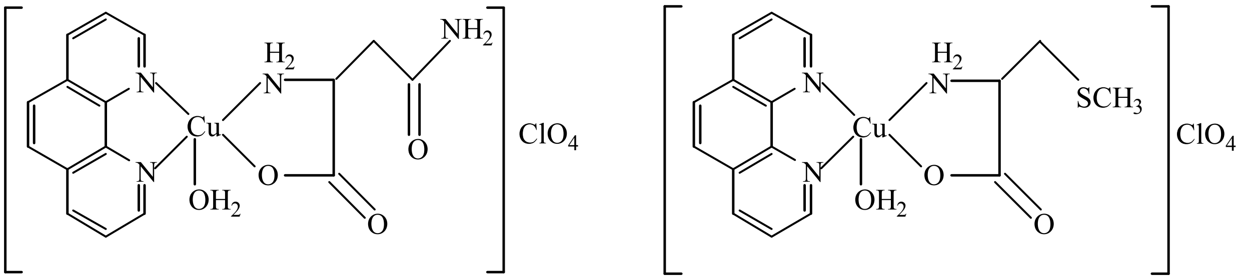

[a] [b]

Figure 1.6: The schematic structures;
a) [Cu^{II} (ternary-L-glutamine)(1,10-phenanthroline)(H_2O)](ClO_4)
b) [Cu^{II}(ternary-S-methyl-L-cysteine)(1,10-phenanthroline)(H_2O)](ClO_4)

$$\begin{aligned}
[\text{M complex}]^{n} + \text{H-MPA} &\longrightarrow [\text{M complex}]^{n-1} + \bullet\text{MPA} + H^{+}\\
[\text{M complex}]^{n-1} + O_2 &\longrightarrow [\text{M complex}]^{n} + \bullet O_2^{-}\\
2\bullet O_2^{-} + 2H^{+} &\longrightarrow H_2O_2 + O_2\\
[\text{M complex}]^{n-1} + H_2O_2 &\longrightarrow [\text{M complex}]^{n} + OH^{-} + \bullet OH\\
[\text{Supercoil DNA}] + \bullet OH &\longrightarrow \text{DNA cleavage}
\end{aligned}$$

Figure 1.7: The proposed DNA cleavage mechanism of metal complex in the presence of 3-mercaptopropionic acid (MPA)

1.3.2 Oxidative DNA cleavage by metal complexes in the presence of ascorbic acid

Complexes $[Ru^{II}(imidazo[4,5-f][1,10]phenanthroline)(NH_3)_4](PF_6)_2$ and $[Cu^{II}(L-threonine)(1,10-phenanthroline)(H_2O)](ClO_4)$ (Figure 1.8) can induce oxidative DNA cleavage in the presence of ascorbic acid [35, 36]. Similar to MPA, ascorbic acid also acts as the reduction agent in the DNA cleavage reaction. Complex $[Ru^{II}(imidazo[4,5-f][1,10]phenanthroline)(NH_3)_4](PF_6)_2$ can only induce single DNA scission by converting supercoil DNA to nicked form while complex $[Cu^{II}(L-threonine)(1,10-phenanthroline)(H_2O)](ClO_4)$ can induce both single and double DNA scissions by converting supercoil DNA to nicked and linear forms. In comparison, complex $[Cu^{II}(L-threonine)(1,10-phenanthroline)(H_2O)](ClO_4)$ appears to be a better DNA cleaver when compared to complex $[Ru^{II}(imidazo[4,5-f][1,10]phenanthroline)(NH_3)_4](PF_6)_2$ in the presence of ascorbic acid. In mechanistic studies, it is evident that the hydroxyl radical scavenger DMSO diminish significantly the nuclease activity of complex $[Cu^{II}(L-threonine)(1,10-phenanthroline)(H_2O)](ClO_4)]$, which is indicative of the involvement of the hydroxyl radical in the cleavage process. The proposed DNA cleavage mechanism of metal complex in the presence of ascorbic acid is illustrated in Figure 1.9.

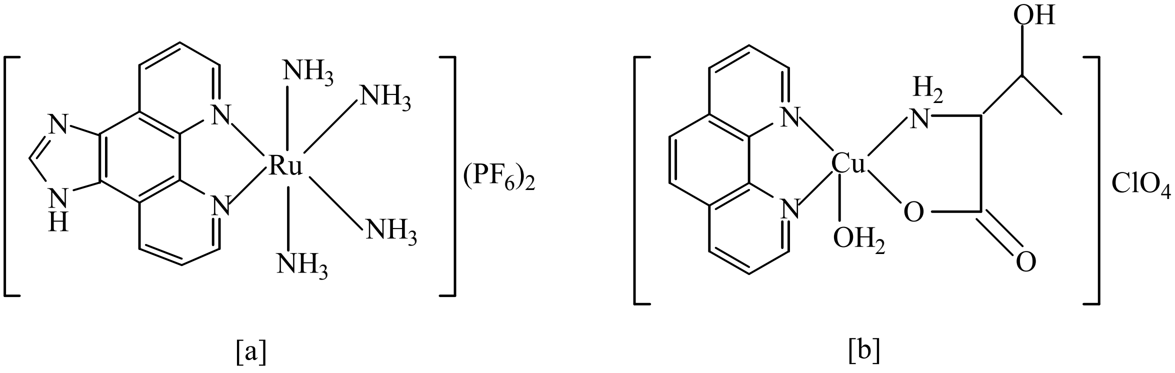

[a]

[b]

Figure 1.8: The schematic structures;
a) $[Ru^{II}(imidazo[4,5\text{-}f][1,10]phenanthroline)(NH_3)_4](PF_6)_2$
b) $[Cu^{II}(L\text{-}threonine)(1,10\text{-}phenanthroline)(H_2O)](ClO_4)$

$$[\text{M complex}]^{n} + \text{H-Asc}^{-} \longrightarrow [\text{M complex}]^{n-1} + \bullet\text{Asc}^{-} + \text{H}^{+}$$

$$[\text{M complex}]^{n-1} + \text{O}_2 \longrightarrow [\text{M complex}]^{n} + \bullet\text{O}_2^{-}$$

$$2\bullet\text{O}_2^{-} + 2\text{H}^{+} \longrightarrow \text{H}_2\text{O}_2 + \text{O}_2$$

$$[\text{M complex}]^{n-1} + \text{H}_2\text{O}_2 \longrightarrow [\text{M complex}]^{n} + \text{OH}^{-} + \bullet\text{OH}$$

$$[\text{Supercoil DNA}] + \bullet\text{OH} \longrightarrow \text{DNA cleavage}$$

Figure 1.9: The proposed DNA cleavage mechanism of metal complex in the presence of ascorbic acid

1.3.3 Oxidative DNA cleavage by metal complexes in the presence of H_2O_2

Complexes $[Co^{II}$(imidazole-terpyridine)$_2](ClO_4)_2$ and $[Cu^{II}$(imidazole terpyridine)$_2](ClO_4)_2$ (Figure 1.10) can promote oxidative DNA cleavage in the presence of H_2O_2 [37, 38]. In contrast to MPA and ascorbic acid, H_2O_2 acts as oxidation agent in the DNA cleavage reaction. Complex $[Co^{II}$(imidazole-terpyridine)$_2](ClO_4)_2$ can only induce single DNA scission by converting supercoil DNA to nicked form while complex $[Cu^{II}$(imidazole terpyridine)$_2](ClO_4)_2$ can induce both single and double DNA scissions by converting supercoil DNA to nicked and linear forms. This indicates that the DNA cleavage efficiency of complex $[Cu^{II}$(imidazole terpyridine)$_2](ClO_4)_2$ is higher than the DNA cleavage efficiency of complex $[Co^{II}$(imidazole-terpyridine)$_2](ClO_4)_2$ in the presence of H_2O_2. From the mechanistic studies, it is shown that the hydroxyl radical scavenger DMSO can reduce significantly the nuclease activity of complex $[Co^{II}$(imidazole-terpyridine)$_2](ClO_4)_2$ while the hydroxyl radical scavenger ethanol can reduce significantly the nuclease activity of complex $[Cu^{II}$(imidazole terpyridine)$_2](ClO_4)_{2.}$ This results reflect that the participation of hydroxyl radical in the cleavage process. The proposed DNA cleavage mechanism of metal complex in the presence of H_2O_2 is illustrated in Figure 1.11.

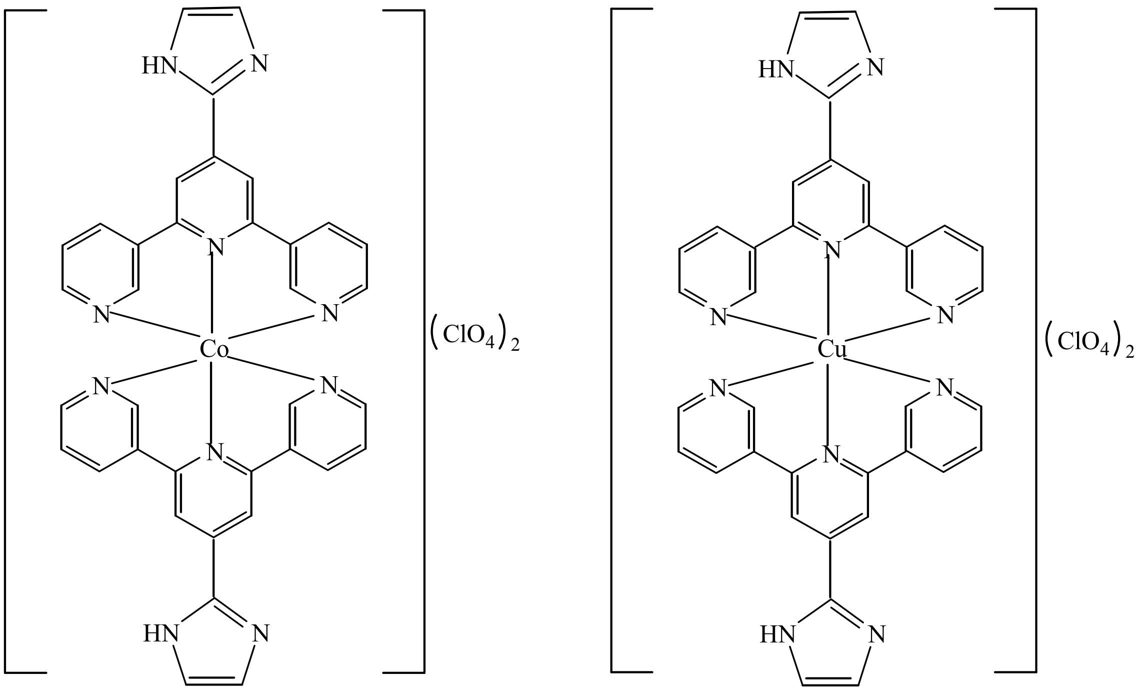

Figure 1.10: The schematic structures;
a) $[Co^{II}(imidazole\text{-}terpyridine)_2](ClO_4)_2$
b) $[Cu^{II}(imidazole\ terpyridine)_2](ClO_4)_2$

$$[\text{M complex}]^{n} + H_2O_2 \longrightarrow [\text{M complex}]^{n-1} + \bullet O_2^{-} + 2H^{+}$$
$$[\text{M complex}]^{n-1} + O_2 \longrightarrow [\text{M complex}]^{n} + \bullet O_2^{-}$$
$$[\text{M complex}]^{n} + \bullet O_2^{-} \longrightarrow [\text{M complex}]^{n-1} + O_2$$
$$[\text{M complex}]^{n-1} + H_2O_2 \longrightarrow [\text{M complex}]^{n} + OH^{-} + \bullet OH$$
$$[\text{Supercoil DNA}] + \bullet OH \longrightarrow \text{DNA cleavage}$$

Figure 1.11: The proposed DNA cleavage mechanism of metal complex in the presence of H_2O_2

1.3.4 Photolytic DNA cleavage by metal complexes

Complexes [Cu^{II}(ternary-S-methyl-L-cysteine)(dipyridoquinoxaline)(H_2O)](ClO_4), [Co^{III} (ethylenediamine)$_2$(imidazo[4,5-f][1,10]-phenanthroline)]Br_3, [Ru^{II}(2,2'-bipyridine)$_2$(5-methoxy-isatino-[1,2-b]-1,4,8,9-tetraazatriphenylene)](ClO_4)$_2$ and [Ni^{II}(naptho[2,3-*a*] dipyrido[3,2-*h*:2',3'-*f*]phenazine-5,18-dione)(1,10-phenanthroline)](PF_6)$_2$ (Figure 1.12) can trigger photolytic DNA cleavage upon irradiation [34, 39, 40, 41]. Complexes [Cu^{II}(ternary-S-methyl-L-cysteine)(dipyridoquinoxaline)(H_2O)](ClO_4) and [Ru^{II}(2,2'-bipyridine)$_2$(5-methoxy-isatino-[1,2-b]-1,4,8,9-tetraaza triphenylene)](ClO_4)$_2$ can induce both single and double DNA scissions by converting supercoil DNA to nicked and linear forms while complexes [Co^{III}(ethylenediamine)$_2$(imidazo[4,5-f][1,10]-phenanthroline)]Br_3 and [Ni^{II}(naptho[2,3-*a*]dipyrido[3,2-*h*:2',3'-*f*]phenazine-5,18-dione)(1,10-phenanthroline)](PF_6)$_2$ can only induce single DNA scission by converting supercoil DNA to nicked form. In comparison, DNA cleavage efficiency of complexes [Ru^{II}(2,2'-bipyridine)$_2$(5-methoxy-isatino-[1,2-b]-1,4,8,9-tetraazatriphenylene)](ClO_4)$_2$ and [Cu^{II}(ternary-S-methyl-L-cysteine)(dipyridoquinoxaline)(H_2O)](ClO_4) is higher than the DNA cleavage efficiency of complexes [Co^{III}(ethylenediamine)$_2$(imidazo)[4,5-f][1,10]-phenanthroline)]Br_3 and [Ni^{II}(naptho[2,3-*a*]dipyrido[3,2-*h*:2',3'-*f*]phenazine-5,18-dione)(1,10-phenanthroline)](PF_6)$_2$ under photolytic DNA cleavage. In mechanistic studies, DNA cleavage activity of complexes [Ru^{II}(2,2'-bipyridine)$_2$(5-methoxy-isatino-[1,2-b]-1,4,8,9-tetraazatriphenylene)](ClO_4)$_2$ and [Cu^{II}(ternary-S-methyl-L-cysteine) (dipyridoquinoxaline)(H_2O)](ClO_4) can be inhibited by singlet oxygen inhibitor sodium azide which indicate the contribution of singlet oxygen in the cleavage process. The DNA cleavage mechanism of the complexes Co^{III}(ethylenediamine)$_2$(imidazo[4,5-

f][1,10]-phenanthroline)]Br_3 and [Ni^{II}(naptho[2,3-*a*]dipyrido[3,2-*h*:2',3'-*f*]phenazine-5,18-dione)(1,10-phenanthroline)]$(PF_6)_2$ is still under investigation. It is proposed that photon from the excitation source excites the metal complexes, which then transfers the energy to the ground state oxygen molecule ($^3O_2$) and excites it to the $^1\Delta g$ state ($^1O_2$). The proposed DNA cleavage mechanism of metal complex under irradiation is illustrated in Figure 1.13.

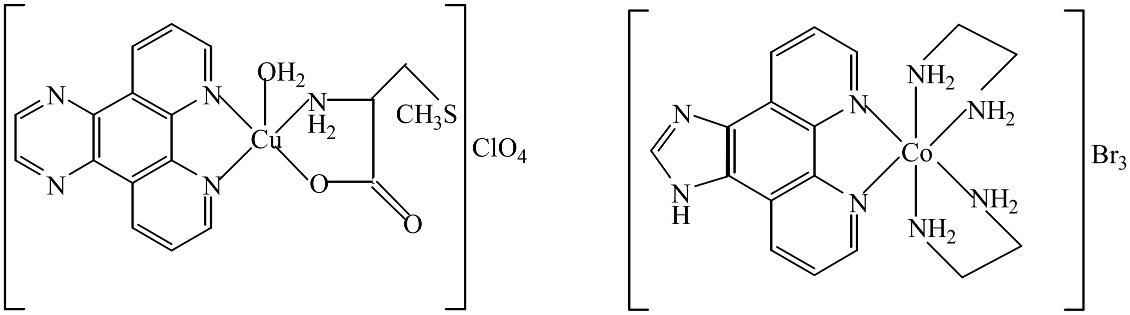

(a)

(b)

Figure1.12: The schematic structures;
a) [Cu^{II}(ternary-S-methyl-L-cysteine)(dipyridoquinoxaline)(H_2O)](ClO_4)
b) [Co^{III}(ethylenediamine)$_2$(imidazo[4,5-f][1,10]-phenanthroline)]Br_3

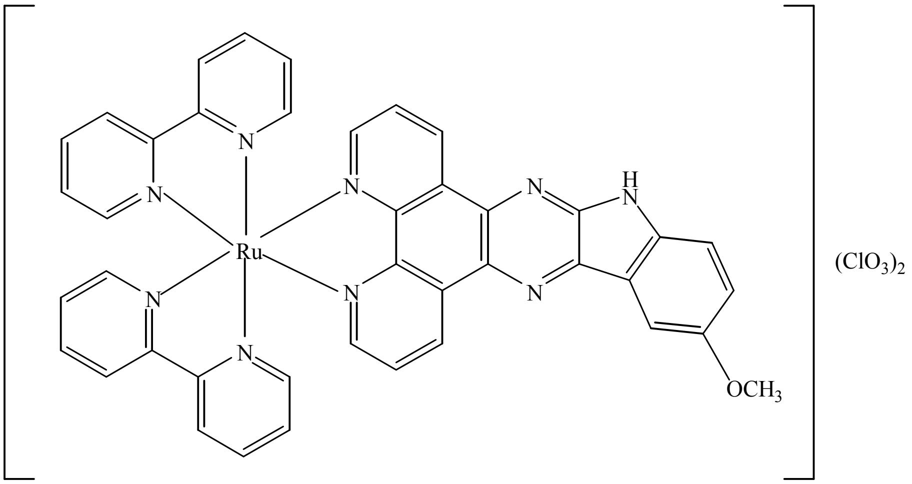

(c)

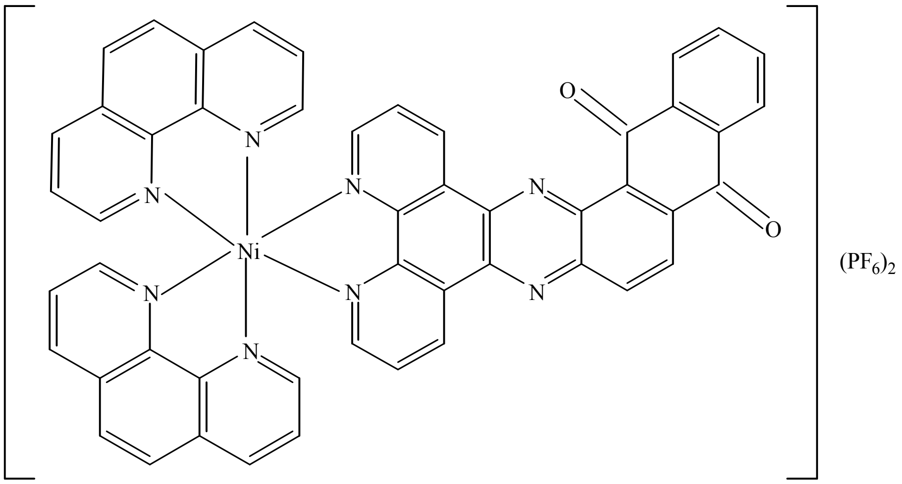

(d)

Figure 1.12: Continued
c) [Ru^{II}(2,2’-bipyridine)$_2$(5-methoxy-isatino-[1,2-b]-1,4,8,9-tetraaza triphenylene)](ClO$_4$)$_2$
d) [Ni^{II}(naptho[2,3-*a*]dipyrido[3,2-*h*:2’,3’-*f*]phenazine-5,18-dione)(1,10-phenanthroline)](PF$_6$)

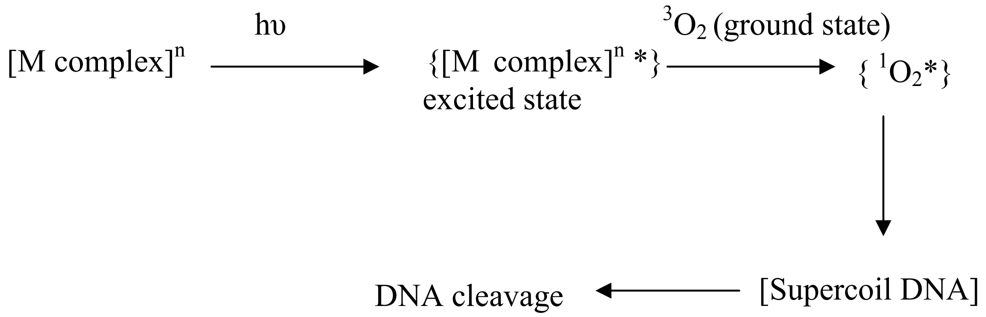

Figure 1.13: The proposed DNA cleavage mechanism of metal complex upon irradiation

1.3.5 Hydrolytic DNA cleavage by metal complexes

Cis-aquahydroxo-tetraamine-cobalt(III) complex, [Co^{III}(bis[2-(2-pyridylethyl)](2-pyridylmethyl)amine)(OH)(H_2O)]$^{2+}$, generated from [Co^{III}(bis[2-(2-pyridylethyl)](2-pyridylmethyl)amine)(CO_3)]ClO_4 and complex [Mn^{II}(quercetin)$_2$(H_2O)$_2$]Cl_2 (Figure 1.14) can induce DNA cleavage via hydrolytic pathway [42, 43]. Both of the complexes can induce DNA cleavage in the absence of co-factor and in the dark. The mechanistic aspects of the DNA cleavage reaction have been investigated with various inhibiting agents and the results show that hydroxyl radical and singlet oxygen scavengers cannot inhibit the DNA cleavage induced by both of the complexes. These observations indicate that hydroxyl radical and singlet oxygen species are not involved in the cleavage reaction. The DNA cleavage characteristics of complexes [Co^{III}(bis[2-(2-pyridylethyl)](2-pyridylmethyl)amine)(OH)(H_2O)]$^{2+}$ and [Mn^{II}(quercetin)$_2$(H_2O)$_2$]Cl_2 support hydrolytic cleavage. Both of the complexes can induce single and double DNA scissions by converting supercoil DNA to nicked and linear forms. In hydrolytic cleavage, it is proposed that DNA cleavage occurs at the P–O bond in the phosphodiester of DNA. The proposed hydrolytic DNA cleavage mechanism by metal complex is illustrated in Figure 1.15.

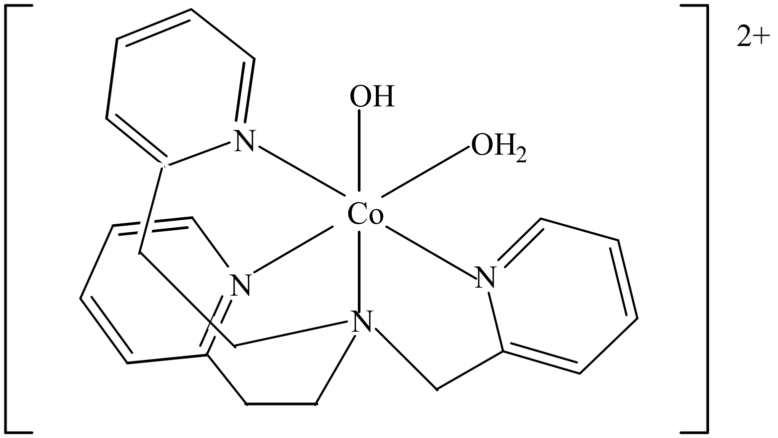

(a)

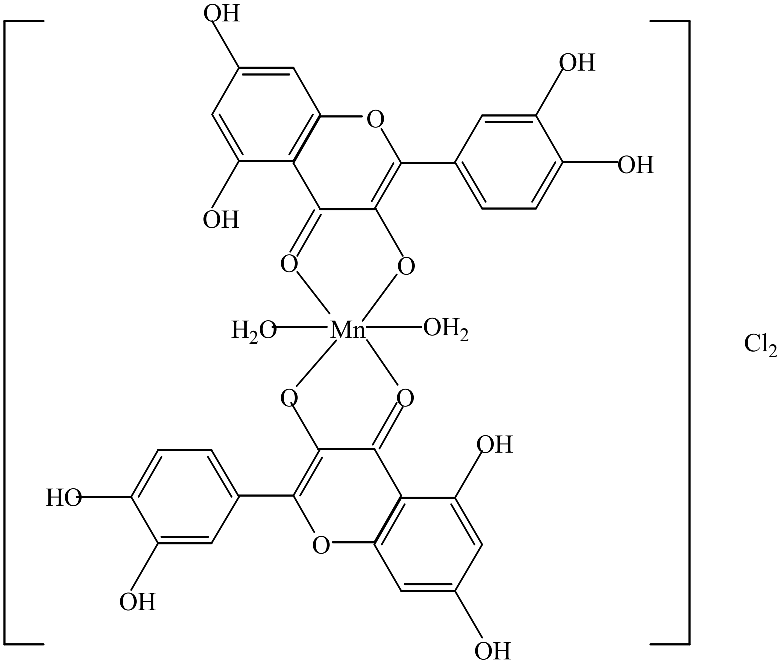

(b)

Figure 1.14: The schematic structures;

a) $[Co^{III}(bis[2\text{-}(2\text{-}pyridylethyl)](2\text{-}pyridylmethyl)amine)(OH)(H_2O)]^{2+}$

b) $[Mn^{II}(quercetin)_2(H_2O)_2]Cl_2$

$$[ML_4(H_2O)(H_2O)]^{n} \xrightarrow{\text{pH 7-8}} [ML_4(H_2O)(HO)]^{n-1} + H^{+}$$

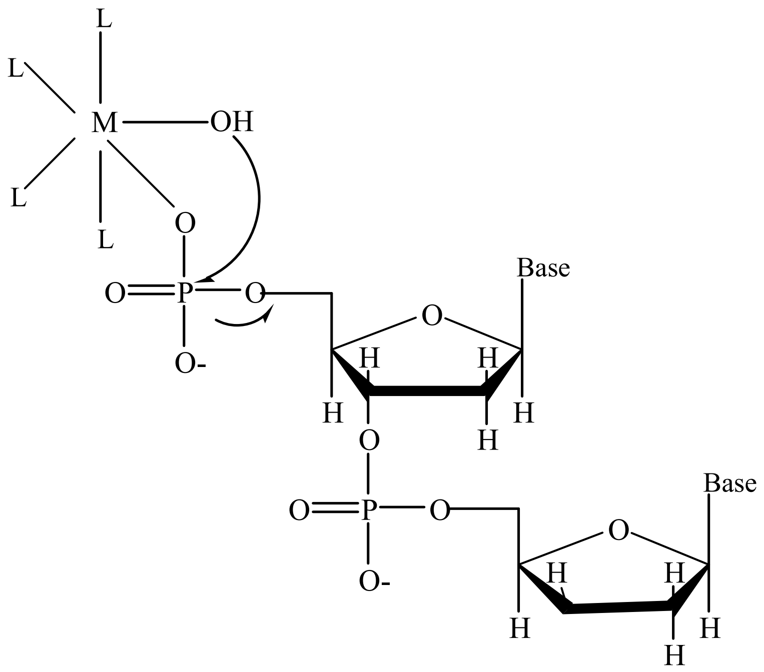

Figure 1.15: The proposed hydrolytic DNA cleavage mechanism by the metal complex

1.3.6 Oxidative DNA cleavage by copper(II) amino acid complexes in the presence of H_2O_2

Recently, Ng et al. have demonstrated that neutral Cu^{II} amino acid complexes such as Cu^{II}(*N,N*-di-(*N*'-methylacetamido)-L-alaninato)$_2$ and Cu^{II}(N,N'-dimethylglycinato)$_2$ (Figure 1.16) can induce oxidative cleavage of DNA in the presence of H_2O_2 [44, 45]. Both of the complexes can induce single and double DNA scissions by converting supercoil DNA to nicked and linear forms. Hydroxyl radical scavenger DMSO can inhibit significantly the cleavage reaction induced by complex Cu^{II}(N,N'-

dimethylglycinato)$_2$ which reflect the involvement of hydroxyl radical in cleavage reaction. The proposed DNA cleavage mechanism by complex Cu^{II}(N,N'-dimethylglycinato)$_2$ is similar to the proposed DNA cleavage mechanism illustrated in Figure 1.11.

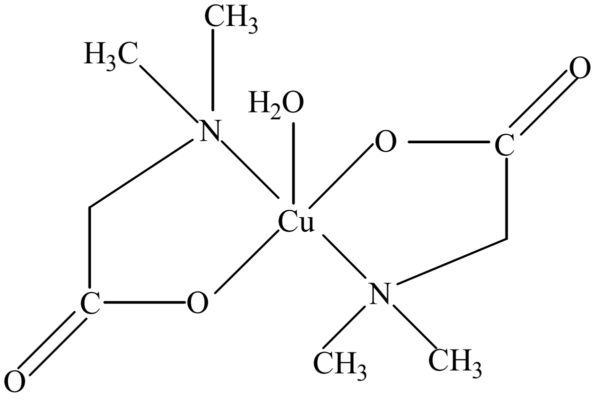

(a)

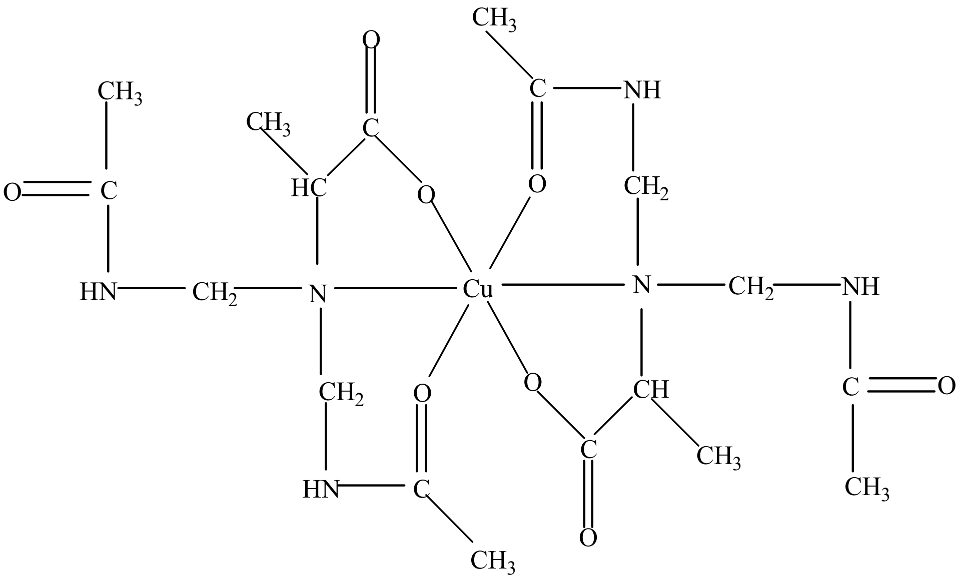

(b)

Figure 1.16: The schematic structures;
a) Cu^{II}(N,N'-dimethylglycinato)$_2$
b) Cu^{II}(*N,N*-di-(*N*'-methylacetamido)-L-alaninato)$_2$